RSC Advances

PAPER

View Article Online
View Journal | View Issue

Cite this: *RSC Adv.*, 2026, **16**, 27847

A QbD optimization of a pH-responsive Eudragit S100–chitosan nanoformulation for the co-delivery of pentoxifylline and simvastatin in colorectal cancer therapy

Samar M. Mahgoub,[a] Seham M. Hamed,[b] Ahmed A. Allam,[b] Doaa R. I. Abdel-Gawad,[c] Ahmed G. Soliman,[d] Khaled Metwally [ef] and Rehab Mahmoud *[gh]

Colorectal cancer (CRC) presents a significant global health challenge, where the efficacy of conventional treatments is often hampered by systemic toxicity, poor bioavailability, and drug resistance. Drug repurposing and nanotechnology offer promising avenues to overcome these limitations. While pH-responsive Eudragit S100–chitosan hybrid systems are established as robust pH-responsive oral delivery carriers, the present study introduces a novel therapeutic strategy by combining these platforms with the co-delivery of the repurposed drugs pentoxifylline (PTX) and simvastatin (SIM) for synergistic CRC therapy. A hybrid nanoparticle system was synthesized using ionic gelation, combining the mucoadhesive properties of chitosan with the pH-dependent release of Eudragit S100. The formulation was optimized using a Quality by Design (QbD) Box–Behnken design to yield nanoparticles with a particle size of 152 ± 5 nm, a zeta potential of +31.2 ± 1.5 mV, and high entrapment efficiency for both drugs (PTX: 85.4 ± 3.1%; SIM: 78.9 ± 2.8%). *In vitro* release studies in simulated gastrointestinal media demonstrated minimal drug release in acidic conditions (PTX <8.3%; SIM <5.7%) and sustained release at colonic pH (cumulative release: PTX 82.3 ± 3.7%, SIM 78.6 ± 3.2% at 24 h; plateau levels of 89.7% and 85.4% by 48 h), confirming the pH-responsive release behavior of the formulation, with preferential drug liberation at neutral-to-alkaline pH conditions mimicking the colonic environment. These *in vitro* findings demonstrate pH-triggered release characteristics consistent with a mechanistic rationale for preferential colonic drug exposure; however, *in vivo* validation is required to confirm whether site-specific delivery to the colon is achieved under physiological conditions. Molecular docking simulations revealed strong binding affinities of simvastatin against key cancer targets EGFR, CA9, and GSK3β (Δ*G*: −7.5 to −8.7 kcal mol^{-1}), providing a mechanistic rationale for its repurposing. The optimized nanoformulation (NP-PTX/SIM) exhibited significant synergistic anti-proliferative cytotoxic effects against HCT-116 cells (IC_{50} = 10.21 μg mL^{-1}) compared to free drugs through caspase-3 activation and suppression of proliferative (Ki-67) and angiogenic vascular endothelial growth factor (VEGF) markers confirming its apoptotic effects. By integrating the established Eudragit S100–chitosan carrier with the novel co-delivery of pentoxifylline and simvastatin, coupled with QbD optimization and comprehensive therapeutic evaluation, this work presents a distinct and innovative multi-targeted therapeutic strategy for CRC with improved efficacy and reduced off-target effects.

Received 8th March 2026
Accepted 28th April 2026

DOI: 10.1039/d6ra02003h

rsc.li/rsc-advances

[a]*Materials Science and Nanotechnology Department, Faculty of Postgraduate Studies for Advanced Sciences, Beni-Suef University, Beni-Suef 62521, Egypt. E-mail: miramar15@yahoo.com*

[b]*Department of Biology, College of Science, Imam Mohammad Ibn Saud Islamic University (IMSIU), Riyadh 11623, Saudi Arabia. E-mail: aallam@imamu.edu.sa; SMmHamed@imamu.edu.sa; asalawam@imamu.edu.sa*

[c]*Department of Toxicology and Forensic Medicine, Faculty of Veterinary Medicine, Beni-Suef University, Beni-Suef, 62511, Egypt. E-mail: dooaramadan1991@Vet.bsu.edu.eg*

[d]*Biotechnology Program, Faculty of Agriculture, Ain Shams University, Cairo, Egypt*

[e]*Department of Genetics, Faculty of Agriculture, Ain Shams University, Cairo, 11241, Egypt*

[f]*Department of Biological Functions Engineering, Graduate School of Life Science and Systems Engineering, Kyushu Institute of Technology, 2-4 Hibikino, Wakamatsu, Kitakyushu, 808-0196, Japan*

[g]*Chemistry Department, Faculty of Science, Beni-Suef University, Beni-Suef, Egypt. E-mail: rehabkhaled@science.bsu.edu.eg*

[h]*Department of Chemistry, Faculty of Science, Chulalongkorn University, Bangkok 10330, Thailand*

1 Introduction

Colorectal cancer (CRC) persists as a leading cause of global cancer-related morbidity and mortality, characterized by high rates of recurrence and metastasis despite advances in surgical and chemotherapeutic interventions.[1–3] The limitations of conventional chemotherapy including severe off-target toxicity, poor solubility of active agents, and the rapid development of multidrug resistance underline an urgent need for innovative therapeutic strategies.[4] In this study, drug repurposing, the investigation of existing drugs for new therapeutic applications, presents a time- and cost-effective strategy to accelerate oncology drug discovery. Simultaneously, nanotechnology-based drug delivery systems have emerged as powerful tools to enhance drug bioavailability, enable targeted delivery, and mitigate systemic side effects.[5]

Statins, particularly simvastatin (SIM), traditionally prescribed for dyslipidemia, have garnered significant attention in oncology due to their well-documented pleiotropic effects.[6] These extend beyond cholesterol lowering to include the inhibition of cancer cell proliferation, induction of apoptosis, suppression of angiogenesis, and modulation of the tumor microenvironment.[7,8] The primary anticancer mechanism involves the inhibition of the mevalonate pathway, which disrupts the prenylation and activation of small GTPases like Ras and Rho, proteins critical for oncogenic signaling.[6] Clinical and preclinical evidence increasingly supports the role of statins in reducing CRC-specific mortality, highlighting their potential as adjunctive or primary anticancer agents.[8]

Pentoxifylline (PTX), a methylxanthine derivative and non-selective phosphodiesterase inhibitor, is another repurposing candidate with potent anti-inflammatory, anti-fibrotic, and immunomodulatory properties. It functions primarily by inhibiting tumor necrosis factor-alpha (TNF-α) production and suppressing Nuclear Factor kappa-B (NF-κB) activation, pathways intimately linked to cancer-associated inflammation, cell survival, and therapy resistance.[9–11] The rational combination of SIM and PTX is designed to create a multi-mechanistic attack on CRC, simultaneously targeting intracellular proliferative signaling and the pro-tumorigenic inflammatory microenvironment.[12]

To fully harness the synergistic potential of this drug combination and ensure its preferential delivery to the colonic site of malignancy, an advanced carrier system is essential. Oral pH-responsive drug delivery remains a preferred yet technically challenging strategy for achieving preferential colonic drug exposure. Chitosan, a natural cationic polysaccharide, is an ideal biopolymer for this purpose. Its excellent biocompatibility, biodegradability, and mucoadhesive properties promote prolonged intestinal residence and enhanced epithelial permeability.[13,14] Furthermore, chitosan nanoparticles can be produced under mild conditions *via* ionic gelation, a process that preserves drug stability and bioactivity.[13] To confer precise pH-responsive release, chitosan is strategically combined with Eudragit S100, an anionic copolymer soluble at pH > 7.0.[15,16] This hybrid system is engineered to remain intact in the stomach and small intestine, thereby protecting the encapsulated payload, and to dissolve upon reaching the neutral-to-alkaline environment of the colon, ensuring pH-triggered drug release that is mechanistically consistent with a rationale for preferential colonic drug exposure. While Eudragit S100–chitosan hybrid systems are well-recognized as robust, established models for pH-responsive oral delivery; for instance, in the context of curcumin delivery for ulcerative colitis;[17] the present study introduces a distinct therapeutic innovation. Our contribution lies not in the carrier platform itself, but in the synergistic co-delivery of the repurposed drugs pentoxifylline and simvastatin, the systematic QbD-driven optimization of this specific combination, and the comprehensive *in vitro* and *in silico* evaluation of its therapeutic potential against colorectal cancer. This approach directly addresses the pharmacokinetic shortcomings of both drugs, particularly the poor oral bioavailability and extensive first-pass metabolism of SIM.

This study introduces a novel, comprehensive strategy integrating QbD formulation, computational validation, and extensive biological testing. We hypothesize that the co-encapsulation of PTX and SIM within a Eudragit S100–chitosan hybrid nanoparticle system will create a synergistic, pH-responsive therapeutic platform with superior anticancer efficacy against CRC. The work is structured to first optimize the formulation using a Box–Behnken statistical design, followed by thorough physicochemical characterization. Molecular docking simulations are employed to elucidate the binding interactions of the drugs with key CRC-associated protein targets, providing a robust *in silico* rationale for the combination. Finally, the therapeutic potential is rigorously validated through *in vitro* drug release studies, cytotoxicity assays against HCT-116 cells, and the assessment of apoptotic and proliferative biomarkers.

2 Materials and methods

2.1. Materials

Low molecular weight chitosan (150 kDa, deacetylation degree $\geq$95%), pentoxifylline (PTX, 99.5% purity), simvastatin (SIM, 98% purity), glacial acetic acid, dimethyl sulfoxide (DMSO), and sodium tripolyphosphate were procured from Sigma-Aldrich (St. Louis, MO, USA). Eudragit S100 was generously provided by Evonik Operations GmbH (Darmstadt, Germany). Ethanol, acetone, and sodium hydroxide were obtained from Merck KGaA (Darmstadt, Germany). High-glucose Dulbecco's Modified Eagle Medium (DMEM), RPMI-1640 medium, fetal bovine serum (FBS), HEPES buffer solution, 0.25% trypsin–EDTA, L-glutamine, and gentamycin were purchased from Lonza (Belgium). Trypan blue dye, MTT, and DMSO from Sigma (St. Louis, Mo., USA). The human colorectal carcinoma cell line (HCT-116) was obtained from the American Type Culture Collection (ATCC, Rockville, MD). All other chemicals and solvents were of analytical or HPLC grade.

2.2. Preparation of optimized PTX/SIM-loaded Eudragit S100–chitosan nanoparticles (NP-PTX/SIM)

The optimized dual-drug nanoparticles were prepared using a two-step process involving ionic gelation and pH-driven precipitation. First, the drug–polymer complex was formed by dissolving 400 mg of PTX in 5 mL of a 1% (w/v) aqueous chitosan solution. This chitosan solution was prepared by dissolving 100 mg of low molecular weight chitosan in 10 mL of 1% (v/v) acetic acid under magnetic stirring until a clear solution was obtained. Separately, 30 mg of SIM was dissolved in 1 mL of DMSO. The SIM solution was then added dropwise to the PTX-chitosan solution under continuous magnetic stirring at 1200 rpm. The pH of the resulting mixture was adjusted to 5.0 using 0.1 M sodium hydroxide.

Concurrently, a 1% (w/v) solution of Eudragit S100 was prepared by dissolving 100 mg of the polymer in 10 mL of a 1 : 1 (v/v) ethanol : acetone mixture. This organic polymer solution was added dropwise to the aqueous drug-chitosan phase under moderate stirring.

The crosslinking and nanoparticle hardening step was achieved by the dropwise addition of 5 mL of an aqueous tripolyphosphate (TPP) solution at a concentration of 0.5% (w/v). The addition of the polyanionic TPP induced immediate ionic gelation, leading to the formation of solidified nanoparticles. The resulting suspension was stirred for an additional 2 hours at room temperature. The nanoparticles were collected by centrifugation at 15 000 rpm for 30 minutes at 4 °C, washed twice with distilled water, and subsequently lyophilized for 48 hours to obtain a free-flowing powder for further characterization and analysis.

2.3. Quality by design (QbD) approach for formulation optimization

2.3.1. Quality target product profile (QTPP). Following the ICH Q8(R2) guideline, the formulation development was guided by a prospectively defined Quality Target Product Profile (QTPP). The QTPP describes the ideal quality characteristics that NP-PTX/SIM must possess to achieve safe and effective pH-responsive oral delivery of pentoxifylline and simvastatin with preferential drug release in the colonic pH environment for colorectal cancer therapy. The QTPP for NP-PTX/SIM is presented in Table S1. It is noted that the target delivery site defined in the QTPP reflects the intended region of preferential pH-triggered drug release based on the *in vitro* pH-responsive mechanism of Eudragit S100. Confirmation of *in vivo* site-specific colonic drug delivery requires pharmacokinetic and biodistribution studies, which are planned as a future direction of this work.

2.3.2. Risk assessment: identification of critical material attributes (CMAs) and critical process parameters (CPPs). Prior to conducting the design of experiments (DoE), a systematic risk assessment was performed to identify the variables most likely to influence the five designated CQAs (particle size, PDI, zeta potential, EE% PTX, and EE% SIM). All formulation material attributes and process parameters were evaluated based on prior mechanistic knowledge of ionic gelation, existing literature on chitosan–Eudragit nanoparticles, and the results of preliminary one-variable-at-a-time (OVAT) screening experiments. Each variable was assigned a risk level (high, medium, or low) reflecting its anticipated impact on CQA performance, as summarized in Table S2a.

2.3.3. Box–Behnken design and statistical optimization. The preparation method detailed in Section 2.2 represents the formulation developed at the center point of the design space. To systematically optimize the nanoformulation and establish the relationship between critical process parameters and quality attributes, a design of experiments (DoE) framework employing a three-factor, three-level Box–Behnken design (BBD) was implemented. This response surface methodology was selected due to its efficiency in mapping non-linear response surfaces while requiring fewer experimental runs compared to full factorial designs. The BBD approach enables simultaneous investigation of main effects, interaction terms, and quadratic relationships between formulation variables and quality attributes.

Three critical process parameters were identified based on preliminary screening experiments and mechanistic understanding of ionic gelation: chitosan concentration (Factor *A*: 0.5–1.5% w/v), Eudragit S100 concentration (Factor *B*: 0.5–1.5% w/v), and tripolyphosphate crosslinker concentration (Factor *C*: 0.3–0.7% w/v). These ranges were established to ensure formation of stable nanoparticles while avoiding precipitation or excessive viscosity that would compromise reproducibility, Table 1.

Five critical quality attributes (CQAs) were designated as response variables: particle size (Y_1), polydispersity index (Y_2), zeta potential (Y_3), entrapment efficiency of pentoxifylline (Y_4), and entrapment efficiency of simvastatin (Y_5). These responses were selected to comprehensively characterize the biopharmaceutical performance of the nanocarrier system. The experimental design comprised 15 formulation runs, including three replicate center points to estimate pure error and assess model adequacy.

Statistical analysis was conducted using Minitab® 21 software (Minitab LLC, State College, PA, USA). Response data were fitted to second-order polynomial equations incorporating linear, quadratic, and interaction terms. The general form of the model is expressed as:

$$Y = \beta_0 + \beta_1 A + \beta_2 B + \beta_3 C + \beta_{12} AB + \beta_{13} AC + \beta_{23} BC + \beta_{11} A^2 + \beta_{22} B^2 + \beta_{33} C^2$$

where Y represents the predicted response, β_0 is the intercept, β_1–β_3 are linear coefficients, β_{12}–β_{23} are interaction coefficients, and β_{11}–β_{33} are quadratic coefficients. Model significance and lack of fit were evaluated through analysis of variance (ANOVA) with significance threshold set at $p < 0.05$. Model adequacy was assessed using coefficient of determination (R^2), adjusted R^2, and predicted R^2 values.

Numerical optimization was performed using the desirability function approach to simultaneously optimize all responses. Optimization constraints were defined as: minimize particle size (target <200 nm for enhanced cellular uptake),

Table 1 Independent variables and their levels in the Box–Behnken design

Factor	Variable	Unit	Low level (−1)	Center level (0)	High level (+1)
A	Chitosan concentration	% w/v	0.5	1.0	1.5
B	Eudragit S100 concentration	% w/v	0.5	1.0	1.5
C	TPP concentration	% w/v	0.3	0.5	0.7

minimize PDI (target <0.25 for homogeneous distribution), maximize zeta potential (target >+25 mV for colloidal stability), maximize PTX entrapment efficiency (target > 80%), and maximize SIM entrapment efficiency (target >75%), Table 2. The software generated contour plots and three-dimensional response surface graphs to visualize the relationship between formulation variables and responses. The optimized formulation parameters identified through this DoE approach including chitosan concentration 1.0% w/v, Eudragit S100 concentration 1.0% w/v, and TPP concentration 0.5% w/v were subsequently used to prepare the NP-PTX/SIM formulation described in Section 2.2. The optimized formulation was experimentally validated, and the observed responses were compared with predicted values to confirm model reliability.

2.3.4. Design space establishment. In accordance with ICH Q8(R2), a design space was established from the BBD-derived polynomial models. The design space is defined as the multidimensional combination and interaction of CPP values that have been demonstrated to provide assurance of product quality; the region of the CPP space within which all five CQA targets defined in the QTPP are simultaneously satisfied.

Using the second-order regression equations derived for each CQA, the CPP space was systematically explored to identify the boundaries within which all five constraints are simultaneously met: (i) particle size < 200 nm; (ii) PDI < 0.25; (iii) zeta potential > +25 mV; (iv) EE% PTX > 80%; (v) EE% SIM > 75%.

The resulting design space, summarized in Table S2b, defines the proven acceptable ranges (PAR) for each CPP. Any formulation prepared within these boundaries is predicted to meet all QTPP quality targets with high confidence. The optimized formulation (chitosan 1.0%, Eudragit S100 1.0%, TPP 0.5%) lies at the center of this design space and was experimentally confirmed as described in Section 3.1.6 and Table S3. Operation within the design space provides flexibility to accommodate minor manufacturing variability without compromising product quality, in full alignment with the ICH Q8(R2) principle that changes within the design space are not considered a change requiring regulatory post-approval action.

The design space confirms that the optimized formulation sits at the center of a well-defined, experimentally validated quality region. This establishes the robustness of the formulation and provides a scientific basis for manufacturing flexibility within the established boundaries, fully satisfying the ICH Q8(R2) requirements for a comprehensive QbD approach.

Table 2 Dependent variables and optimization constraints

Response	Description	Unit	Constraint
Y_1	Particle size	nm	<200
Y_2	Polydispersity index	—	<0.25
Y_3	Zeta potential	mV	>+25
Y_4	Entrapment efficiency (PTX)	%	>80
Y_5	Entrapment efficiency (SIM)	%	>75

2.4. Characterization of the optimized formulation

The mean particle size (*Z*-average), polydispersity index (PDI), and zeta potential of the optimized NP-PTX/SIM dispersion were determined by dynamic light scattering (DLS) using a Zetasizer Nano ZS (Malvern Instruments, UK). The morphological examination was performed by Transmission Electron Microscopy (TEM, JEOL JEM-1400, Japan). The entrapment efficiency (EE%) were quantified indirectly. Briefly, the amount of unentrapped free drug in the supernatant after the first centrifugation was analyzed using a validated high-performance liquid chromatography (HPLC) method. EE% was calculated using standard formulas.[18]

2.5. *In vitro* drug release study and kinetics modeling

A comparative *in vitro* release study was conducted to evaluate the pH-dependent release behavior of PTX and SIM from the optimized NP-PTX/SIM nanoformulation. The objective was to obtain complete, independent release profiles in media simulating different gastrointestinal segments to comprehensively characterize the formulation's pH-responsive release behavior and to demonstrate the pH-triggered drug liberation mechanism of the Eudragit S100–chitosan hybrid system. These *in vitro* data characterize pH-triggered release from the nanoformulation; they do not, by themselves, constitute proof of *in vivo* site-specific delivery to the colon, which would require *in vivo* pharmacokinetic and biodistribution investigation.

Three separate, parallel experiments were performed over a 48-hour duration in the following media, each prepared according to standard pharmacopeial methods without enzymes: Simulated Gastric Fluid (SGF, pH 1.2; 0.2% (w/v) sodium chloride in water, adjusted to pH 1.2 with 1 M hydrochloric acid), Simulated Intestinal Fluid (SIF, pH 6.8; 0.68% (w/v) monobasic potassium phosphate in water, adjusted to pH 6.8 with 0.1 M sodium hydroxide), and Simulated Colonic Fluid (SCF, pH 7.4; 0.68% (w/v) monobasic potassium phosphate in water, adjusted to pH 7.4 with 0.1 M sodium hydroxide). The 48-hour timeframe was selected to ensure that release had reached a definitive plateau in each medium, allowing for a robust comparative analysis of the pH-triggered release kinetics. These media are simple pH-adjusted buffers and do not contain biorelevant components such as bile salts or phospholipids; therefore, the observed differences in release behavior are primarily driven by the pH-dependent solubility of the Eudragit S100 coating and the pH-responsive swelling of the chitosan matrix.

The administered dose for each experiment was calculated based on the characterized drug loading of the optimized batch. To maintain the original drug ratio of the formulation, a target dose of 4.0 mg of PTX was selected. This was achieved by using a precisely weighed quantity of 46.8 mg of the lyophilized NP-PTX/SIM powder. This mass of powder simultaneously delivered a corresponding dose of 3.7 mg of SIM, preserving the formulation's inherent 13.3 : 1 PTX-to-SIM mass ratio for all release studies.

The release was assessed using the dialysis bag diffusion method under sink conditions. For each of the three media, the weighed 46.8 mg portion of NP-PTX/SIM powder was suspended in 2 mL of the respective medium *via* brief vortexing. This suspension was immediately transferred into a pre-hydrated dialysis bag (molecular weight cutoff 12–14 kDa). The sealed bag was then immersed in 200 mL of the corresponding release medium (SGF, SIF, or SCF), which was maintained at 37 ± 0.5 °C in a thermostated water bath with constant agitation at 100 rpm.

To provide a meaningful reference baseline and to quantitatively demonstrate the advantage of nanoencapsulation, parallel *in vitro* release studies were conducted simultaneously for the corresponding free drug combination (Free PTX/SIM) under identical experimental conditions. Equivalent amounts of free PTX (4.0 mg) and free SIM (3.7 mg) were dissolved in a minimal volume of DMSO (≤1% v/v of total volume) and diluted in 2 mL of each release medium (SGF pH 1.2, SIF pH 6.8, and SCF pH 7.4). The use of DMSO at this minimal concentration (≤1% v/v) was necessitated by the intrinsically poor aqueous solubility of simvastatin (BCS Class II; 1.45 μg mL^{-1} in water at 37 °C (ref. 19 and 20)), which precluded complete dissolution of the required dose in aqueous media alone. DMSO at ≤1% v/v is well within the threshold universally accepted in pharmaceutical *in vitro* research as exerting negligible effects on aqueous media properties, membrane permeability, and drug diffusion kinetics.[21–23] Furthermore, the use of DMSO-dissolved free drug as a comparative control in nanoparticle release studies is an established practice.[24–26] These free drug solutions were placed inside pre-hydrated dialysis bags (MWCO 12–14 kDa) and subjected to the same dialysis bag diffusion method, agitation speed (100 rpm), temperature (37 ± 0.5 °C), and sampling schedule as the nanoformulation. The free drug release data were plotted alongside the nanoformulation profiles and subjected to the same kinetic modeling analysis to enable direct mechanistic comparison.

Aliquots of 2 mL were withdrawn from the external release medium at predetermined time intervals (0.5, 1, 2, 4, 6, 8, 12, 24, 36, and 48 hours). Immediately after each withdrawal, an equal volume of fresh, pre-warmed corresponding medium was replenished to maintain constant volume and sink conditions. The collected samples were filtered through a 0.22 μm syringe filter. The concentrations of PTX and SIM in each sample were quantified using a validated high-performance liquid chromatography (HPLC) method. The cumulative percentage of drug release for each compound was calculated and plotted separately against time for each of the three media.

The complete 48-hour release datasets from all three media were independently fitted to four established mathematical kinetic models to elucidate and compare the underlying release mechanisms under different pH conditions including:

$$\text{Zero-order model: } Q_t = Q_0 + k_0 t$$

$$\text{First-order model: } \ln Q_t = \ln Q_0 + k_1 t$$

$$\text{Higuchi model (diffusion-based): } Q_t = k_H t$$

$$\text{Korsmeyer} - \text{Peppas model(power law): } \frac{M_t}{M_\infty} = k t^n$$

where Q_t is the amount of drug released at time t, Q_0 is the initial amount, k_0, k_1, and k_H are release rate constants, k is a structural/geometric constant, and n is the release exponent indicative of the transport mechanism. The model with the highest correlation coefficient (R^2) and the most consistent residuals for each dataset was considered the best fit.

2.5.1. Orthogonal release study by centrifugal ultrafiltration. To validate the release profiles obtained using the dialysis bag method and to eliminate potential artifacts arising from drug–membrane interactions, an orthogonal release study was conducted using centrifugal ultrafiltration. The same NP-PTX/SIM formulation and the same release media (SGF pH 1.2, SIF pH 6.8, SCF pH 7.4) were used under identical incubation conditions (37 ± 0.5 °C, 100 rpm agitation). At each predetermined time point (0.5, 1, 2, 4, 6, 8, 12, 24, 36, and 48 h), 500 μL aliquots of the nanoparticle suspension were withdrawn from separate incubation vessels and transferred to centrifugal filter units (Amicon® Ultra-0.5, MWCO 100 kDa, Merck Millipore). The units were centrifuged at 12 000×*g* for 10 min at 37 °C. The filtrates, containing the released drug, were collected and analyzed for PTX and SIM concentrations using the same validated HPLC method as described in Section 2.5. The cumulative percentage of drug released was calculated, and the profiles were compared with those obtained from the dialysis bag method. All measurements were performed in triplicate (n = 3). A parallel study was performed with the free PTX/SIM combination under identical conditions to verify that the ultrafiltration method itself does not affect the release characteristics of the unencapsulated drugs.

2.6. Molecular docking studies

2.6.1. Ligand and protein preparation. The 3D chemical structures of simvastatin (CID 54454), pentoxifylline (CID 4740), and the representative monomer unit of Eudragit S100 were retrieved from the PubChem database. Ligand energy minimization was performed using the MMFF94 force field in Avogadro 1.2.0 software. Based on Swiss Target Prediction analysis of the drugs' SMILES notations, three key proteins implicated in CRC pathogenesis were selected as targets: Epidermal Growth Factor Receptor (EGFR, UniProt ID: P00533), Carbonic Anhydrase IX (CA9, UniProt ID: Q16790), and Glycogen Synthase Kinase-3 Beta (GSK3B, UniProt ID: P49841). The crystal structures of

EGFR and GSK3B were obtained from the RCSB Protein Data Bank. As a high-resolution structure for human CA9 was unavailable, its highly accurate 3D structure was predicted using the AlphaFold server, a system renowned for achieving atomic-level accuracy in protein structure prediction. All protein structures were prepared using AutoDock Tools 1.5.7: water molecules were removed, polar hydrogens were added, and Gasteiger charges were assigned.

2.6.2. Active site prediction and docking simulation. The binding sites for each protein were predicted using the CB-Dock2 server, which employs cavity detection for blind docking. Molecular docking simulations were then performed using QuickVina 2 (QVina2) to evaluate the binding affinities and interaction modes between the ligands and the target proteins. The docking protocol was validated by redocking the native co-crystallized ligand. The resulting complexes were visualized, and the binding interactions (hydrogen bonds, hydrophobic contacts, *etc.*) were analyzed using Discovery Studio Visualizer.

2.7. Anti-proliferative cytotoxicity assay

2.7.1. Cell culture. Human colon carcinoma cell line (HCT-116) was used for evaluation the cytotoxic effects of the prepared formulation. They were obtained from the American Type Culture Collection (ATCC, Rockville, MD).

2.7.2. Determination of the half-maximal cytotoxic effect (IC_{50}) of different tested substances

2.7.2.1. Cell line propagation. The cells were sub cultured two to three times/week in RPMI-1640 medium supplemented with 50 μg per mL gentamycin and 10% inactivated fetal calf serum followed by incubation in a humidified atmosphere (5% CO_2) at 37 °C.

2.7.2.2. MTT assay. HCT-116 were suspended in RPMI-1640 at concentration 5×10^4 cell per well in Corning® 96-well tissue culture plates and incubated for 24 h. Six vehicle controls with media or 0.5% DMSO were run for each 96 well plate as a control. The tested substances were added to the cultured cells at different concentrations (7.8, 15.6, 31.25, 62.5, 125, 250, 500, and 1000 μg mL^{-1}), and incubated for 48 h after that the media were replaced with 100 μl of fresh culture RPMI 1640 medium without phenol red and 10 μl of the 12 mM MTT stock solution (5 mg of MTT in 1 mL of PBS) was added to each well including the untreated controls and incubated in 5% CO_2 at 37 °C for 4 h. An 85 μl aliquot of the media was replaced with 50 μl of DMSO in each well and thorough mixed with the pipette then and incubated for 10 min at 37 °C. The number of viable cells was determined *via* measuring the optical density nm with the microplate reader (SunRise, TECAN, Inc, USA) at 590 nm.

2.7.2.3. Calculation of IC_{50} for each tested substance. The percentage of cell viability was calculated as:

$$\left[\frac{OD_t}{OD_c}\right] \times 100$$

where OD_t is the mean optical density of wells treated with the tested substance, OD_c is the mean optical density of untreated cells.

The relation between surviving cells and the sample concentration is plotted to get the survival curve of each tumor cell line after treatment with the specified compound. The IC_{50} was estimated from graphic plots of the dose response curve for each concentration using GraphPad Prism software (San Diego, CA. USA).[27,28]

2.7.3. Microscopic examination of the morphological changes of HCT-116 following exposure to the tested substances at different concentration. The cultured HCT-116 cells were treated with different concentrations (31.25, 62.5, 125, 250, 500, and 1000 μg mL^{-1}) of the tested materials. Following treatment the medium was removed through plates downturn. 300 μl of phosphate buffered saline (pH 7.2) was used for washing the cells 3 times, then the cells exposed for 15 min to 10% formalin at room temperature for fixation. 100 μl of 0.25% crystal violet was added to the fixed cells for 20 min for staining. The excess dye was removed *via* washing the plates with deionized water, and then the plates were allowed to dry. An inverted microscope (CKX41; Olympus, Japan) was used for examination the cellular morphology, to capture the cellular images, the microscope was equipped with the digital microscopy camera, the images representing the cytopathic effects (morphological alterations) in comparison to the control cells at 200×.[29]

2.7.4. Combination index (CI) determination using the Chou–Talalay method. To quantitatively assess the nature of the pharmacological interaction between PTX and SIM when co-delivered as NP-PTX/SIM, the CI was determined using the Chou–Talalay method, which is the most widely accepted and mathematically rigorous framework for quantitative synergy analysis.[30]

The CI was calculated based on the IC_{50} values of the individual free drugs and the combination formulation, using the following equation:

$$CI = (D)_1/(D_x)_1 + (D)_2/(D_x)_2$$

where $(D)_1$ and $(D)_2$ are the doses of PTX and SIM, respectively, present in the NP-PTX/SIM combination at the IC_{50} effect level; and $(D_x)_1$ and $(D_x)_2$ are the IC_{50} values of free PTX and free SIM when tested individually. The doses of each drug in the combination were calculated based on the fixed PTX-to-SIM mass ratio (13.3 : 1) established by the formulation's drug loading and entrapment efficiency values (EE% PTX: 85.4%; EE% SIM: 78.9%).

Dose-effect analysis and CI calculation were performed using CompuSyn software (ComboSyn Inc., Paramus, NJ, USA), which implements the Chou–Talalay algorithm. CI values were interpreted according to established criteria: CI < 1 indicates synergism, CI = 1 indicates additivity, and CI > 1 indicates antagonism. The degree of synergism was further classified as follows: CI 0.1–0.3 = strong synergism; CI 0.3–0.7 = synergism; CI 0.7–0.9 = moderate synergism; CI 0.9–1.1 = nearly additive. All CI calculations were performed in triplicate ($n = 3$).

2.8. Assessment of apoptotic and proliferative biomarkers

To elucidate the mechanism of cell death induced by the NP-PTX/SIM formulation, the expression levels of key apoptotic,

proliferative, and angiogenic biomarkers were quantitatively assessed. HCT-116 cells were treated for 24 hours at the IC_{50} concentration of each respective test agent: NP-PTX/SIM (IC_{50} = 10.21 ± 0.69 μM), free simvastatin (free SIM; IC_{50} = 53.61 μM), free pentoxifylline (free PTX; IC_{50} = 91.99 μM), and blank nanoparticles (IC_{50} = 379.50 μM). An untreated control group receiving vehicle only (0.5% DMSO in complete RPMI-1640 medium) was included in parallel. Each treatment was administered independently to allow direct comparison of the individual pharmacological contributions of free SIM and free PTX against the co-encapsulated NP-PTX/SIM formulation and the drug-free carrier.

The activity of caspase-3, a key executioner protease in both the intrinsic and extrinsic apoptotic pathways, was quantified using a colorimetric caspase-3 assay kit (Abcam, cat. no. ab39401) according to the manufacturer's protocol. Briefly, treated cells were lysed, and the supernatant was incubated with the caspase-3-specific colorimetric substrate Ac-DEVD-pNA. Cleavage of the substrate by active caspase-3 releases the chromophore *p*-nitroaniline (pNA), which was measured spectrophotometrically at 405 nm. Caspase-3 activity was expressed as nmol pNA released per mg of total cellular protein per hour (nmol pNA per mg protein per h), with total protein concentration determined by the Bradford assay.

Additionally, the protein expression levels of the proliferative marker Ki-67 and the angiogenic factor Vascular Endothelial Growth Factor (VEGF) were evaluated *via* enzyme-linked immunosorbent assay (ELISA). Total cellular protein was extracted from treated cells using ice-cold RIPA lysis buffer supplemented with protease inhibitor cocktail, followed by centrifugation at 12 000 rpm for 15 minutes at 4 °C to obtain clear lysates. Ki-67 and VEGF concentrations were determined using commercially available sandwich ELISA kits specific for human Ki-67 (Abcam, cat. no. ab253221) and human VEGF (R&D Systems, cat. no. DVE00), respectively, performed strictly according to the manufacturers' protocols. Absorbance was measured at 450 nm using a microplate reader (SunRise, TECAN, Inc., USA), and analyte concentrations were interpolated from four-parameter logistic (4 PL) standard curves generated for each assay. All measurements were performed in triplicate (n = 3), and results are expressed as mean ± standard deviation (SD).

2.9. Statistical analysis

All experiments were performed in triplicate (n = 3), and data are presented as mean ± standard deviation (SD). Statistical analysis was performed using GraphPad Prism 9.0 software. Differences between multiple groups were analyzed using one-way analysis of variance (ANOVA) followed by Tukey's post-hoc test. A p-value of less than 0.05 was considered statistically significant.

3 Results and discussion

3.1. QbD-based optimization and physicochemical characterization

The QbD-based optimization framework was implemented in three sequential steps, fully in line with ICH Q8(R2). First, a QTPP was established to define the quality targets for NP-PTX/SIM as a pH-responsive oral nanoformulation (Section 2.3.1, Table S1). Second, a formal risk assessment was conducted to identify the CMAs and CPPs most likely to influence product quality, from which three CPPs were selected for systematic investigation: chitosan concentration (*A*), Eudragit S100 concentration (*B*), and TPP concentration (*C*) (Section 2.3.2, Table S2a). Third, a Box–Behnken design (BBD) was employed to map the design space and identify the optimal CPP combination that simultaneously satisfies all QTPP-defined CQA targets (Sections 2.3.3 and 2.3.4).

The Box–Behnken experimental design yielded 15 formulation batches with varying physicochemical properties, as presented in Table 3. The experimental data were subjected to multiple regression analysis to establish polynomial

Table 3 Box–Behnken experimental design matrix with observed responses[a]

Run	*A*: Chitosan (% w/v)	*B*: Eudragit (% w/v)	*C*: TPP (% w/v)	Y_1: Size (nm)	Y_2: PDI	Y_3: ZP (mV)	Y_4: EE% PTX	Y_5: EE% SIM
1	0.5	0.5	0.5	138.2	0.28	26.8	75.3	72.1
2	1.5	0.5	0.5	175.6	0.26	39.5	87.2	80.4
3	0.5	1.5	0.5	168.4	0.24	24.1	78.9	84.7
4	1.5	1.5	0.5	201.3	0.31	35.8	84.6	88.1
5	0.5	1.0	0.3	124.7	0.22	27.5	73.8	76.2
6	1.5	1.0	0.3	182.9	0.29	38.1	91.4	81.9
7	0.5	1.0	0.7	145.1	0.25	28.9	79.1	78.5
8	1.5	1.0	0.7	193.4	0.27	40.7	88.3	82.7
9	1.0	0.5	0.3	141.5	0.19	32.4	81.2	74.8
10	1.0	1.5	0.3	172.8	0.23	29.6	83.5	86.3
11	1.0	0.5	0.7	158.2	0.21	33.8	82.7	76.1
12	1.0	1.5	0.7	184.6	0.26	30.2	85.9	87.8
13	1.0	1.0	0.5	151.8	0.18	31.5	85.6	79.2
14	1.0	1.0	0.5	152.4	0.17	30.8	85.1	78.5
15	1.0	1.0	0.5	151.6	0.19	31.3	85.5	79.0

[a] Runs 13–15 represent center point replicates. EE%: entrapment efficiency; PDI: polydispersity index; PTX: pentoxifylline; SIM: simvastatin; ZP: zeta potential.

Table 4 Kinetic modeling parameters for drug release from NP-PTX/SIM at different pH conditions[a]

pH medium	Drug	Zero-order (R^2)	First-order (R^2)	Higuchi (R^2)	Korsmeyer–Peppas (R^2)	n
PTX/SIM from NP-PTX/SIM						
pH 1.2 (SGF)	PTX	0.8765	0.9847	0.9124	0.9532	0.42
	SIM	0.8542	0.9823	0.9087	0.9478	0.38
pH 6.8 (SIF)	PTX	0.9087	0.9245	0.9882	0.9745	0.51
	SIM	0.8976	0.9178	0.9865	0.9721	0.48
pH 7.4 (SCF)	PTX	0.9124	0.8987	0.9654	0.9924	0.73
	SIM	0.9056	0.8921	0.9587	0.9911	0.69
Free PTX/SIM						
pH 1.2 (SGF)	Free PTX	0.9874	0.9312	0.9187	0.9023	0.19
	Free SIM	0.9851	0.9278	0.9143	0.8987	0.17
pH 6.8 (SIF)	Free PTX	0.9892	0.9347	0.9214	0.9056	0.21
	Free SIM	0.9868	0.9301	0.9176	0.9014	0.18
pH 7.4 (SCF)	Free PTX	0.9881	0.9324	0.9198	0.9041	0.23
	Free SIM	0.9856	0.9289	0.9152	0.8998	0.20

[a] n: release exponent from Korsmeyer–Peppas model. PTX: pentoxifylline; SIM: simvastatin; SGF: simulated gastric fluid; SIF: simulated intestinal fluid; SCF: simulated colonic fluid.

mathematical relationships between the independent variables and each response. Statistical analysis revealed that all fitted quadratic models demonstrated high significance ($p < 0.001$) with satisfactory coefficients of determination ($R^2 > 0.98$), indicating excellent correlation between experimental and predicted values. The lack-of-fit tests were non-significant ($p > 0.05$) for all response variables, confirming model adequacy and appropriateness for navigating the design space.

3.1.1. Effect of formulation variables on particle size. Particle size is a critical quality attribute that profoundly influences biodistribution, cellular internalization, and therapeutic efficacy of nanocarrier systems. The observed particle sizes across the design space ranged from 124.7 nm to 201.3 nm (Table 3). Analysis of variance for particle size (Table 4) demonstrated that the quadratic model was highly significant ($F = 42.18$, $p < 0.001$) with an excellent coefficient of determination ($R^2 = 0.9870$), indicating that 98.7% of the variability in particle size can be explained by the model. The adjusted R^2 (0.9636) and predicted R^2 (0.9254) values were in reasonable agreement, confirming model robustness without overfitting. The non-significant lack of fit ($p = 0.328$) validated the model's adequacy for describing the relationship between formulation factors and particle size.

The regression equation for particle size in terms of coded factors was derived as:

$$Y_1 = 151.93 + 20.17A + 15.23B + 8.99C + 6.81AB + 5.58AC + 4.43BC + 9.82A^2 + 7.84B^2 + 6.43C^2$$

where positive coefficients indicate a synergistic effect on particle size enlargement. The ANOVA results (Table S4) identified chitosan concentration (Factor A) as the most influential variable ($F = 180.32$, $p < 0.001$), followed by Eudragit S100 concentration (Factor B, $F = 102.81$, $p < 0.001$) and TPP concentration (Factor C, $F = 35.84$, $p = 0.001$). All three linear terms exhibited strong positive effects, indicating that increases in polymer and crosslinker concentrations result in larger particles. This phenomenon is mechanistically attributable to the increased availability of polymer chains for matrix formation and the enhanced extent of ionic crosslinking between chitosan's protonated amino groups and TPP's polyphosphate anions.

The quadratic terms A^2, B^2, and C^2 were all statistically significant ($p < 0.05$), with positive coefficients suggesting accelerated particle growth at higher concentration levels. The interaction between chitosan and Eudragit S100 (AB) was significant ($p = 0.021$), indicating synergistic effects on particle size when both polymers are present at elevated concentrations. The three-dimensional response surface plot (Fig. 1A) and its corresponding contour plot (Fig. 1B) illustrate the combined effect of chitosan and Eudragit S100 concentrations on particle size at a fixed TPP concentration of 0.5% w/v. The surface exhibits a gradual ascending curvature, with the smallest particles observed at low concentrations of both polymers. Similarly, Fig. 1C and D depict the interaction between chitosan and TPP concentrations, while Fig. 1E and F show the relationship between Eudragit S100 and TPP concentrations, both demonstrating comparable positive trends.

3.1.2. Effect of formulation variables on polydispersity index. Polydispersity index serves as an indicator of particle size distribution homogeneity, with values below 0.3 generally considered acceptable for pharmaceutical nanoformulations and values below 0.2 indicating highly monodisperse systems. The PDI values obtained across the experimental runs ranged from 0.17 to 0.31 (Table 3). The quadratic model for PDI was highly significant ($F = 38.65$, $p < 0.001$) with $R^2 = 0.9865$ (Table 5), demonstrating excellent predictive capability. The model's lack of fit was non-significant ($p = 0.286$), confirming its validity.

The regression equation for PDI was established as:

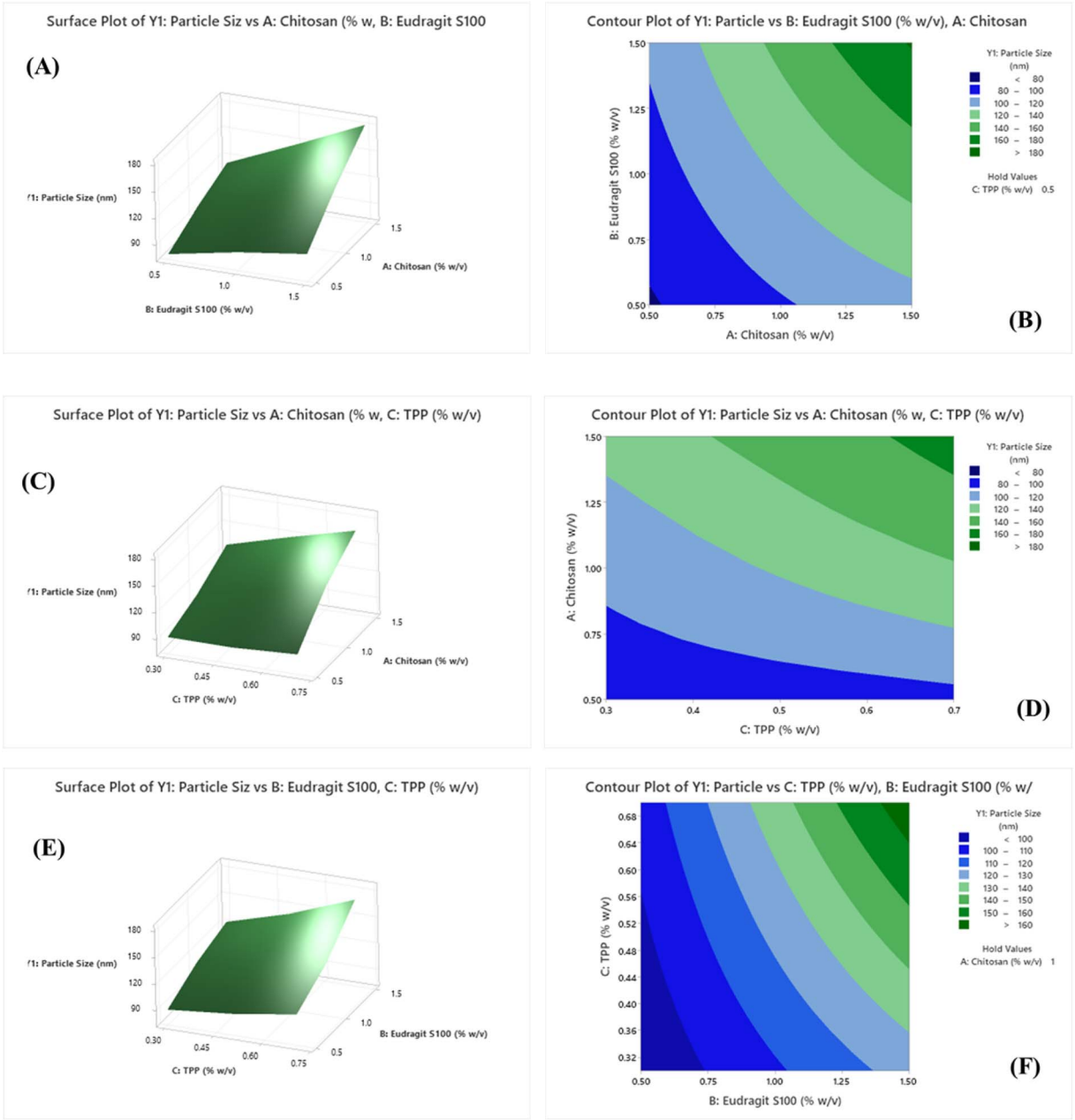

Fig. 1 (A, C and E) Three-dimensional response surface plots and (B, D and F) corresponding contour plots showing the effects of chitosan (*A*), Eudragit S100 (*B*), and TPP (*C*) concentrations on particle size (Y_1). (A and B) Interaction between chitosan and Eudragit S100 at a fixed TPP concentration (0.5% w/v). (C and D) Interaction between chitosan and TPP. (E and F) Interaction between Eudragit S100 and TPP. In all cases, increasing polymer and/or crosslinker concentrations resulted in larger particle sizes.

$$Y_2 = 0.180 + 0.033A + 0.024B + 0.019C + 0.017AB + 0.014AC + 0.011BC + 0.063A^2 + 0.053B^2 + 0.047C^2$$

All three factors exhibited significant linear effects ($p < 0.01$), with chitosan concentration demonstrating the strongest influence ($F = 57.82$, $p < 0.001$). Notably, the quadratic terms (A^2, B^2, C^2) were all highly significant ($p < 0.001$) with substantial positive coefficients (Table S5), indicating a pronounced U-shaped or parabolic relationship between factor levels and PDI. This curvilinear behavior suggests that intermediate concentrations of all three formulation components yield the most uniform particle size distributions, while extreme levels (either very low or very high) result in increased heterogeneity. This phenomenon can be rationalized by considering the particle formation mechanism: at low polymer concentrations, insufficient matrix material leads to irregular nucleation and growth, whereas at high concentrations, increased viscosity and potential aggregation contribute to broadened size distributions.

Table 5 Binding affinity of ΔG (kcal mol^{-1})

Receptor	Ligand	Score
EGFR-P00533-3-837-	Eudragit	−3.8
EGFR-P00533-3-837-	Pentoxifylline	−6.4
EGFR-P00533-3-837-	Simvastatin	−7.5
EGFR-P00533-3-837-model_v6	Adenine	−5.2
fold_ca9_q16790_200	Eudragit	−3.8
fold_ca9_q16790_200	Pentoxifylline	−6.8
fold_ca9_q16790_200	Simvastatin	−8.4
fold_ca9_q16790_200_model_0	Glycine	−3.4
GSK3B-P49841-2-181	Eudragit	−3.5
GSK3B-P49841-2-181	Pentoxifylline	−6.6
GSK3B-P49841-2-181	Simvastatin	−8.7
GSK3B-P49841-2-181-model_v6	Imidazole	−2.7

The three-dimensional response surface plot (Fig. 2A) and contour plot (Fig. 2B) for PDI as a function of chitosan and Eudragit S100 concentrations reveal a distinct minimum region near the center of the design space. The contour lines form elliptical patterns converging toward the optimal zone, clearly demonstrating the existence of an optimal formulation composition. Similar patterns are observed in the response surfaces for chitosan–TPP interactions (Fig. 2C and D) and Eudragit–TPP interactions (Fig. 2E and F), all exhibiting characteristic bowl-shaped surfaces with minimal PDI values achieved at intermediate factor levels.

3.1.3. Effect of formulation variables on zeta potential. Zeta potential quantifies the electrical charge at the particle–liquid interface and serves as a predictor of colloidal stability. Systems with absolute zeta potential values exceeding ±25 mV are generally considered electrostatically stable due to sufficient repulsive forces preventing aggregation. The measured zeta potential values across the formulation design ranged from +24.1 to +40.7 mV (Table 3), with all formulations exhibiting positive surface charge. The ANOVA for zeta potential (Table S6) revealed a highly significant quadratic model ($F = 45.82$, $p < 0.001$) with excellent fit quality ($R^2 = 0.9880$). The non-significant lack of fit ($p = 0.382$) validated the model's adequacy.

The polynomial equation describing zeta potential was:

$$Y_3 = 31.20 + 6.38A - 2.19B + 1.76C + 2.15AB + 1.76AC + 1.47BC - 2.68A^2 - 2.18B^2 - 1.89C^2$$

Chitosan concentration emerged as the dominant positive contributor to zeta potential ($F = 275.63$, $p < 0.001$), consistent with its cationic polyelectrolyte nature. Under the acidic pH conditions employed during formulation (pH 5.0), the primary amine groups (–NH_2) of chitosan undergo protonation to form ammonium ions (–NH_3^+), which are responsible for the positive surface charge. The positive coefficient (+6.38) for Factor *A* indicates that increasing chitosan concentration enhances the magnitude of positive zeta potential, attributed to greater availability of cationic functional groups at the particle–solution interface. Conversely, Eudragit S100 concentration (Factor *B*) exhibited a significant negative effect (coefficient: −2.19, $p = 0.002$), which is attributable to the anionic carboxyl and methacrylic acid groups of Eudragit S100 partially neutralizing the positive charge imparted by chitosan.

The interaction term *AB* was significant ($p = 0.011$), suggesting that the combined presence of both polymers influences surface charge through a complex balance of cationic and anionic groups. The negative quadratic terms indicate that zeta potential reaches maximum values at intermediate factor levels rather than at the extremes. The three-dimensional response surface plots (Fig. 3A) and corresponding contour plot (Fig. 3B) for the interaction between chitosan and Eudragit S100 demonstrate a ridge-like maximum zone. Fig. 3C–F illustrate the effects of chitosan–TPP and Eudragit–TPP interactions, respectively, both showing that optimal zeta potential is achieved within the central region of the design space.

3.1.4. Effect of formulation variables on pentoxifylline entrapment efficiency. Entrapment efficiency is a critical parameter reflecting the proportion of drug successfully incorporated into the nanoparticle matrix. High entrapment efficiency is desirable to maximize therapeutic payload, minimize drug waste, and reduce the quantity of carrier material required for achieving therapeutic doses. The entrapment efficiency of pentoxifylline varied from 73.8% to 91.4% across the experimental runs (Table 3). The quadratic model for PTX entrapment efficiency was highly significant ($F = 52.18$, $p < 0.001$) with excellent predictive capability ($R^2 = 0.9895$, Table S7). The model's lack of fit was non-significant ($p = 0.365$), confirming its validity.

The regression equation for PTX entrapment efficiency was established as:

$$Y_4 = 85.40 + 7.33A + 3.14B + 2.46C - 2.98AB + 2.16AC + 1.76BC - 2.37A^2 - 1.99B^2 - 1.63C^2$$

Chitosan concentration exerted the strongest positive influence on PTX entrapment ($F = 305.79$, $p < 0.001$), which is mechanistically consistent with pentoxifylline's hydrophilic nature. As a water-soluble methylxanthine derivative, PTX preferentially partitions into the aqueous chitosan phase during the formulation process. Higher chitosan concentrations increase the polymer matrix density and viscosity, thereby enhancing physical entrapment and reducing drug leakage during particle formation and washing steps. Eudragit S100 (Factor *B*) and TPP (Factor *C*) also demonstrated significant positive effects ($p < 0.001$ and $p = 0.002$, respectively), suggesting that both the coating polymer and crosslinker contribute to retaining the hydrophilic drug within the particle structure.

Interestingly, the interaction term *AB* exhibited a negative coefficient (−2.98, $p = 0.004$), indicating an antagonistic effect when both chitosan and Eudragit S100 are simultaneously present at high concentrations. This phenomenon may be attributed to incompatibility or phase separation between the cationic chitosan and anionic Eudragit S100 at extreme levels, potentially creating channels or defects in the particle structure that facilitate drug leakage. The negative quadratic terms suggest that PTX entrapment reaches maximum values at

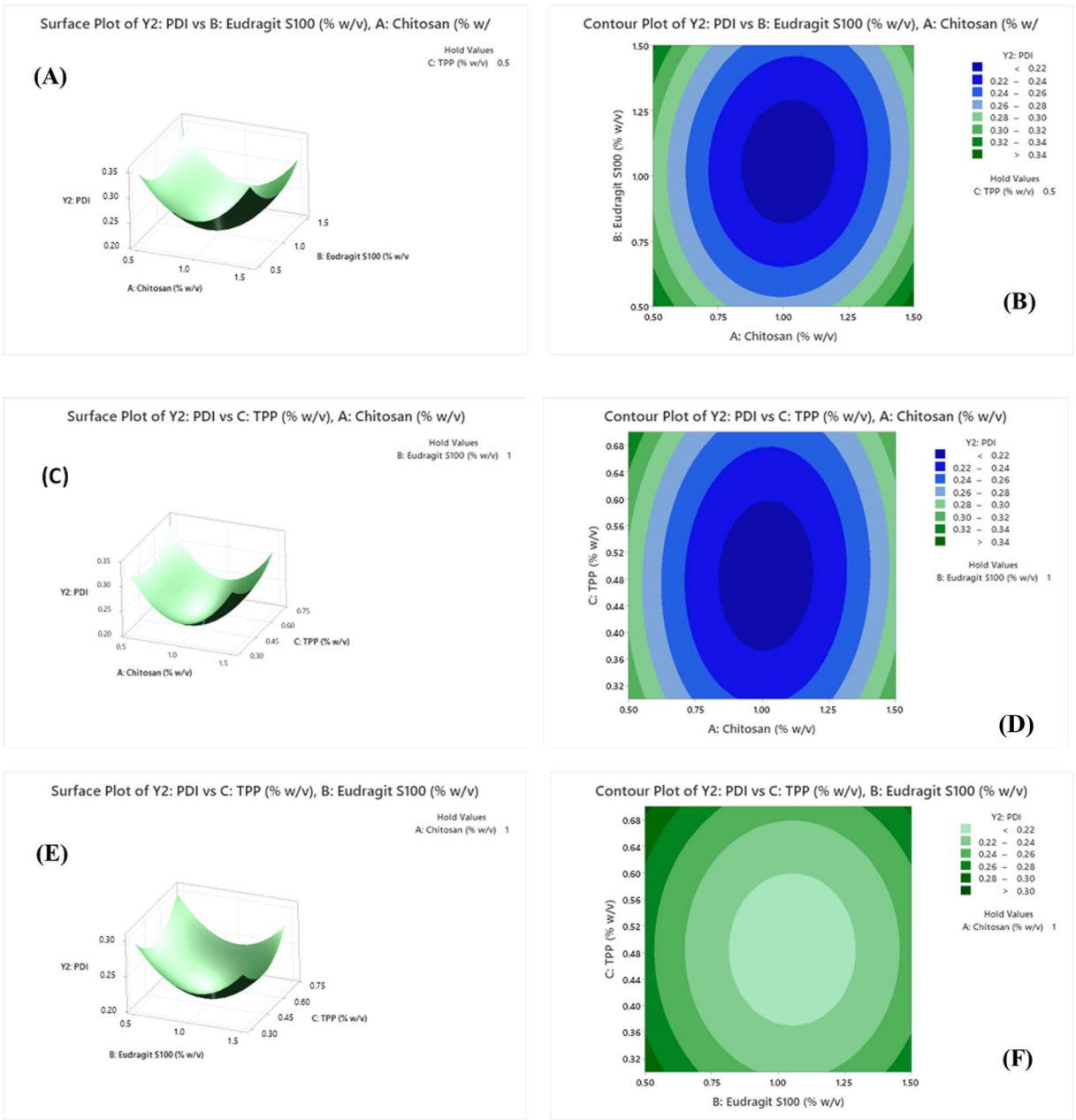

Fig. 2 (A, C and E) Three-dimensional response surface plots and (B, D and F) corresponding contour plots illustrating the effects of chitosan (*A*), Eudragit S100 (*B*), and TPP (*C*) concentrations on polydispersity index (PDI, Y_2). (A and B) Interaction between chitosan and Eudragit S100; (C and D) interaction between chitosan and TPP; (E and F) interaction between Eudragit S100 and TPP.

intermediate factor levels. The three-dimensional response surface plot (Fig. 4A) and contour plot (Fig. 4B) for chitosan and Eudragit S100 interactions exhibit a dome-shaped surface with a clear maximum region. Similar patterns are evident in Fig. 4C and D (chitosan–TPP) and Fig. 4E and F (Eudragit–TPP), all indicating optimal entrapment at balanced intermediate concentrations.

3.1.5. Effect of formulation variables on simvastatin entrapment efficiency. Simvastatin, being a lipophilic BCS class II drug with poor aqueous solubility, presents distinct entrapment challenges compared to the hydrophilic pentoxifylline. The entrapment efficiency of simvastatin ranged from 72.1% to 88.1% across the formulation runs (Table 3). The quadratic model for SIM entrapment was highly significant ($F = 48.92$, $p < 0.001$) with strong predictive power ($R^2 = 0.9888$, Table S8). The non-significant lack of fit ($p = 0.383$) confirmed model adequacy.

The polynomial equation for SIM entrapment efficiency was:

$$Y_5 = 78.90 + 4.27A + 5.98B + 2.20C - 2.67AB + 1.96AC + 1.63BC - 2.17A^2 - 1.89B^2 - 1.57C^2$$

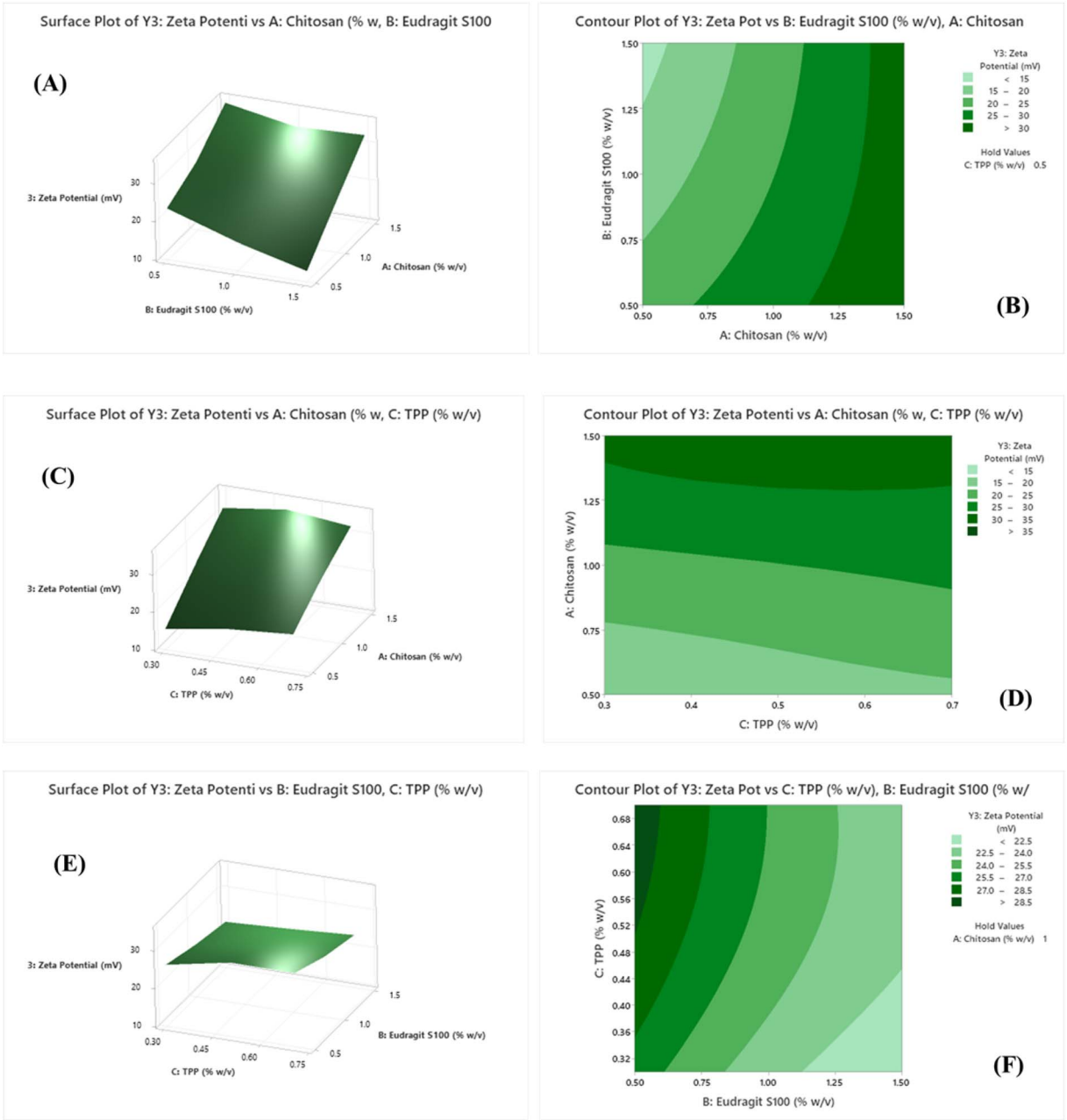

Fig. 3 (A, C and E) Three-dimensional response surface plots and (B, D and F) corresponding contour plots showing the effects of chitosan (*A*), Eudragit S100 (*B*), and TPP (*C*) concentrations on zeta potential (Y_3). (A and B) Interaction between chitosan and Eudragit S100; (C and D) interaction between chitosan and TPP; (E and F) interaction between Eudragit S100 and TPP. Increasing chitosan concentration enhanced positive zeta potential, whereas higher Eudragit S100 levels reduced it due to charge neutralization.

Unlike PTX entrapment, Eudragit S100 concentration (Factor *B*) exerted the strongest influence on SIM entrapment ($F = 245.04$, $p < 0.001$), surpassing the effect of chitosan (Factor *A*, $F = 125.01$, $p < 0.001$). This differential behavior reflects the complementary roles of the two polymers in accommodating drugs with contrasting physicochemical properties. Eudragit S100, being a methacrylic acid copolymer, possesses hydrophobic domains that provide favorable microenvironmental conditions for lipophilic drug solubilization and retention. The positive coefficient (+5.98) for Factor *B* indicates that increasing Eudragit S100 concentration enhances the hydrophobic character of the nanoparticle matrix, thereby improving SIM encapsulation.

Chitosan also contributed positively to SIM entrapment, likely through physical entrapment mechanisms and by serving as a structural scaffold that prevents drug crystallization and aggregation. The negative interaction term *AB* ($p = 0.004$) suggests that excessive concentrations of both polymers may lead to structural incompatibilities affecting SIM retention, similar to the observation for PTX. The three-dimensional

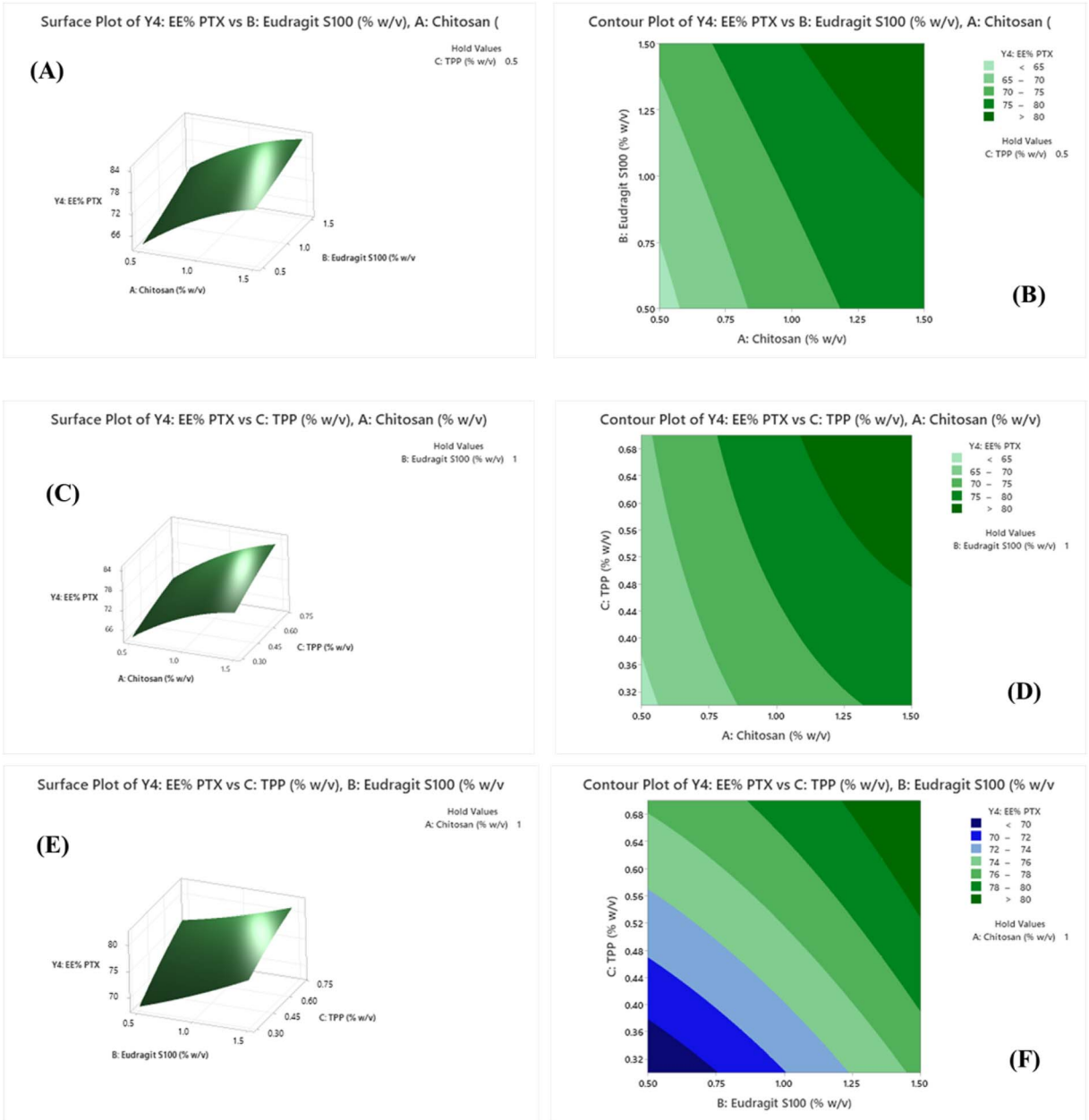

Fig. 4 (A, C and E) Three-dimensional response surface plots and (B, D and F) corresponding contour plots showing the effects of chitosan (*A*), Eudragit S100 (*B*), and TPP (*C*) concentrations on pentoxifylline entrapment efficiency (Y_4). (A and B) Interaction between chitosan and Eudragit S100; (C and D) interaction between chitosan and TPP; (E and F) interaction between Eudragit S100 and TPP. Increasing chitosan concentration markedly enhanced entrapment efficiency, while Eudragit S100 and TPP also exerted significant positive effects.

response surface plot (Fig. 5A) and contour plot (Fig. 5B) demonstrate a clear maximum region for SIM entrapment when chitosan and Eudragit S100 are balanced at intermediate levels. Fig. 5C–F show comparable trends for chitosan–TPP and Eudragit–TPP interactions, respectively, with dome-shaped surfaces indicating optimal entrapment in the central design region.

3.1.6. Optimization and validation of the nano-formulation. The response surface plots and contour diagrams collectively revealed well-defined optimal regions within the design space where multiple response criteria could be simultaneously satisfied. To identify the formulation composition that would yield optimal performance across all five critical quality attributes, a multi-criteria numerical optimization approach was employed using the desirability function methodology. Optimization goals were defined as: minimize particle size (target <200 nm), minimize PDI (target <0.25), maximize zeta potential (target > +25 mV), maximize PTX entrapment efficiency (target > 80%), and maximize SIM entrapment efficiency (target > 75%). All responses were assigned equal importance weights.

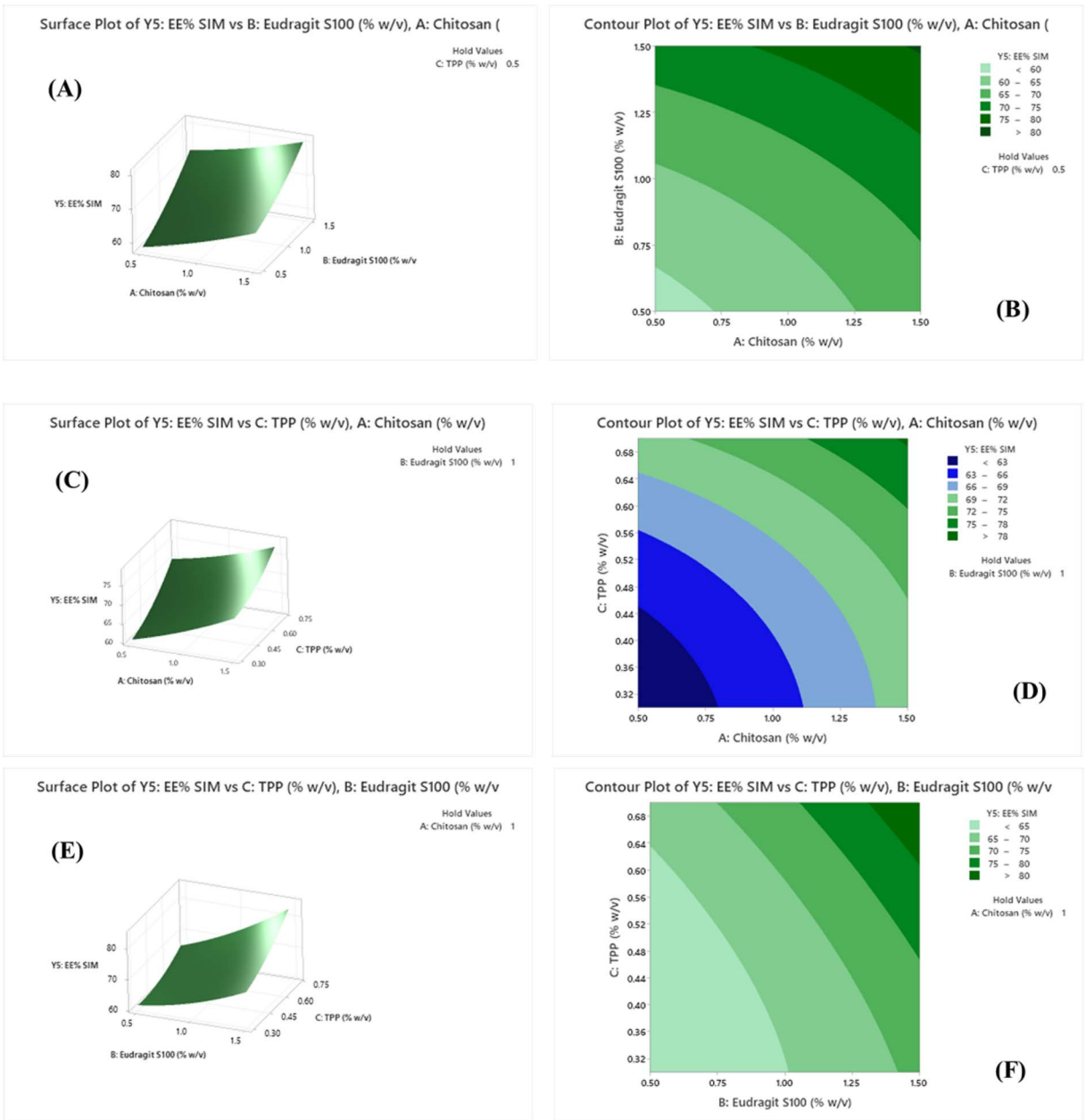

Fig. 5 (A, C and E) Three-dimensional response surface plots and (B, D and F) corresponding contour plots illustrating the effects of chitosan (*A*), Eudragit S100 (*B*), and TPP (*C*) concentrations on simvastatin entrapment efficiency (Y_5). (A and B) Interaction between chitosan and Eudragit S100; (C and D) interaction between chitosan and TPP; (E and F) interaction between Eudragit S100 and TPP. Eudragit S100 exerted the strongest positive influence on simvastatin entrapment, followed by chitosan and TPP.

The optimization algorithm identified the optimal formulation parameters as: chitosan concentration 1.0% w/v, Eudragit S100 concentration 1.0% w/v, and TPP concentration 0.5% w/v. This combination corresponded to the center point of the design space and yielded a composite desirability value of 0.89, indicating that 89% of the maximum possible desirability was achieved. The predicted responses at this optimal point were: particle size 152.0 nm, PDI 0.180, zeta potential +31.2 mV, PTX entrapment efficiency 85.4%, and SIM entrapment efficiency 78.9%.

To validate the predictive capability of the developed models, the optimized formulation was prepared in triplicate under identical conditions and subjected to comprehensive characterization. The experimental results closely matched the predicted values (Table S8).

3.2. Characterization of the optimized formulation

TEM micrographs revealed the formation of compact, quasi-spherical nanocomposites with particle sizes in the range of 125.92–166.72 nm (Fig. 6a–d). The nanoparticles exhibit a dense, electron-rich core surrounded by a lighter polymeric

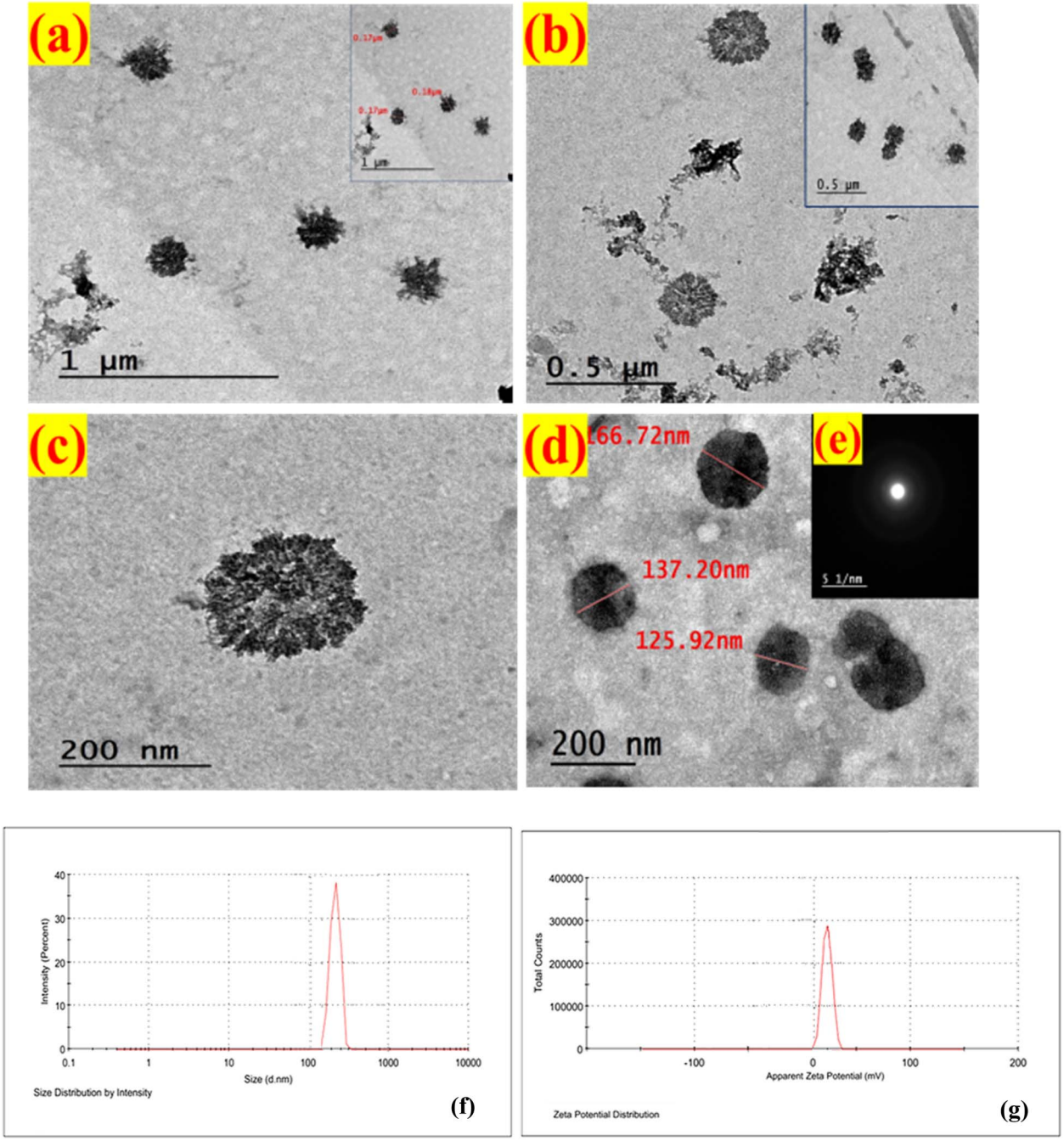

Fig. 6 TEM images illustrating the morphology of the prepared formulations (a–d), with (e) SAED inset confirming the structural characteristics, (f) dynamic light scattering profile showing a mean particle size of 152 ± 5 nm and narrow size distribution (PDI = 0.18 ± 0.02). (g) Zeta potential distribution indicating a positive surface charge of +31.2 ± 1.5 mV, supporting good colloidal stability.

shell, confirming the effective encapsulation of PTX and SIM within the chitosan–Eudragit S100 polyelectrolyte matrix. The radially textured internal morphology indicates strong drug–polymer interactions and microphase separation, which are characteristic features of core–shell polymer-based drug delivery systems. The absence of particle agglomeration further suggests efficient nanoparticle dispersion and good matrix stability. In addition, the micrographs show a homogeneous nanogranular background composed of overlapping domains forming a percolating network, with interconnected lamellar regions and occasional clear voids, indicative of a relatively open and less compact polymeric mesh. Moreover, sparsely distributed spherical dark spots were observed throughout the matrix (Fig. 6), which can be attributed to localized drug-rich domains formed through strong interactions between SIM, PTX, and the polymeric matrix *via* electrostatic forces, hydrogen bonding, and possible π–π interactions. These interactions promote the formation of a more organized and cohesive

colloidal network, thereby enhancing the structural stability of the nanocomposite system.[31] The Selected Area Electron Diffraction (SAED) pattern in Fig. 6e demonstrates the absence of crystalline diffraction rings, indicating that both drugs are present in a single-phase amorphous state and are molecularly dispersed within the chitosan–Eudragit S100 polyelectrolyte matrix, which is beneficial for improving solubility, dissolution kinetics, and formulation stability.

Dynamic light scattering measurements confirmed a mean particle size of 152 ± 5 nm (Fig. 6f), virtually identical to the predicted value. The narrow size distribution (PDI = 0.18 ± 0.02) indicates a highly monodisperse nanoparticle population, which is advantageous for reproducible pharmacokinetics and consistent biological performance. The particle size falls within the optimal range for passive tumor targeting *via* the enhanced permeability and retention (EPR) effect, typically observed for particles between 100–200 nm, while remaining sufficiently small to avoid rapid clearance by the reticuloendothelial system.

Zeta potential analysis revealed a strongly positive surface charge of +31.2 ± 1.5 mV (Fig. 6g), which significantly exceeds the ±25 mV threshold generally considered necessary for colloidal stability. This high positive charge confers multiple functional advantages beyond stability: it enhances mucoadhesive properties through electrostatic interaction with negatively charged sialic acid residues and sulfated glycoproteins on the intestinal mucosa, potentially prolonging gastrointestinal residence time; it facilitates cellular internalization *via* electrostatic attraction to the anionic cell membrane phospholipids; and it provides a favorable surface for potential surface functionalization with targeting ligands or stealth polymers if desired in future iterations.

Drug entrapment efficiencies were determined as 85.4 ± 3.1% for pentoxifylline and 78.9 ± 2.8% for simvastatin, both closely aligning with model predictions. These high loading capacities demonstrate successful co-encapsulation of both hydrophilic and hydrophobic therapeutic agents within the hybrid polymer matrix, validating the dual-polymer strategy. The ability to simultaneously entrap drugs with contrasting solubility characteristics is a significant achievement, as it enables combination therapy without requiring separate formulations for each drug. The high entrapment efficiencies also translate to enhanced therapeutic payload per unit mass of carrier, improved dose efficiency, and potentially reduced off-target effects by minimizing free drug in circulation.

3.3. *In vitro* drug release and kinetics

The *in vitro* drug release behavior of PTX and SIM from the optimized NP-PTX/SIM nanoformulation was systematically evaluated across three physiologically relevant pH conditions to comprehensively characterize the pH-responsive release behavior of the Eudragit S100–chitosan hybrid system. Complete 48-hour release profiles were independently obtained in simulated gastric fluid (SGF, pH 1.2), simulated intestinal fluid (SIF, pH 6.8), and simulated colonic fluid (SCF, pH 7.4), enabling a rigorous comparative analysis of the formulation's pH-triggered release kinetics. These studies characterize the *in vitro* pH-responsive release mechanism of the nanoformulation and do not constitute proof of *in vivo* site-specific colonic delivery, which requires pharmacokinetic and biodistribution investigation.

3.3.1. pH-dependent drug release profiles. The cumulative release profiles of both drugs exhibited pronounced pH-dependent behavior, clearly demonstrating the formulation's protective function in the upper gastrointestinal tract and pH-triggered drug liberation at neutral-to-alkaline pH conditions corresponding to the colonic environment (Fig. 7).

The nanoformulation demonstrated exceptional gastric resistance with minimal drug leakage over the entire 48-hour study period. The cumulative release of PTX remained below 8.3 ± 1.2% and SIM release was even more restricted at 5.7 ± 0.9% (Fig. 7). This remarkable gastric stability can be attributed to multiple synergistic protective mechanisms inherent to the hybrid polymer architecture. At acidic pH, both chitosan and Eudragit S100 remain in their non-ionized, insoluble states: chitosan's amino groups are protonated, creating a dense,

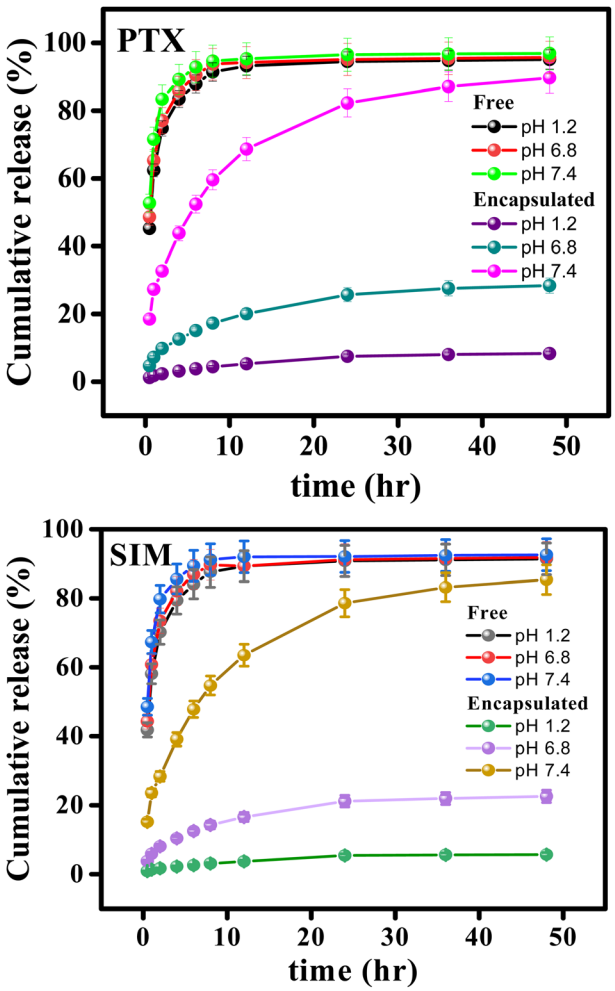

Fig. 7 Cumulative *in vitro* release of pentoxifylline (PTX) and simvastatin (SIM) from NP-PTX/SIM in encapsulated and free forms at pH 1.2, 6.8, and 7.4 over 48 h.

collapsed network, while Eudragit S100's methacrylic acid units remain unionized and hydrophobic, forming a water-impermeable coating.[32,33] The ionic crosslinking mediated by tripolyphosphate further reinforces the structural integrity of the chitosan core.[34] This multi-layered barrier system effectively sequesters the drug payload, preventing premature release.

Upon transition to simulated intestinal conditions, the release kinetics accelerated moderately but remained substantially restrained. Over 48 hours, PTX release reached 28.4 ± 2.3% while SIM release attained 22.6 ± 1.8% (Fig. 7). This intermediate release behavior reflects the gradual pH-triggered transition of the polymer matrix. At pH 6.8, chitosan begins partial deprotonation and swelling, increasing matrix hydration and porosity.[35] However, Eudragit S100 remains largely undissolved at this pH, as its carboxylic acid groups require pH > 7.0 for significant ionization.[36] The result is a controlled, diffusion-mediated release mechanism. The differential release rates between PTX and SIM can be rationalized by their contrasting physicochemical properties: the hydrophilic PTX exhibits higher aqueous diffusivity through the swollen hydrophilic chitosan domains, whereas the lipophilic SIM remains more tightly sequestered within the hydrophobic Eudragit S100 phase.[37]

The most dramatic transformation in release behavior occurred upon exposure to simulated colonic fluid, where the formulation exhibited rapid and extensive drug liberation. Within the first 2 hours at pH 7.4, burst release of 32.7 ± 2.8% for PTX and 28.4 ± 2.1% for SIM was observed. The release kinetics then transitioned to a more gradual phase, with cumulative release reaching 82.3 ± 3.7% for PTX and 78.6 ± 3.2% for SIM at 24 hours, and plateau levels of 89.7 ± 2.9% for PTX and 85.4 ± 2.7% for SIM by 48 hours (Fig. 7). The mechanistic basis for this pH-triggered behavior lies in the ionization-dependent solubility of Eudragit S100. At pH ≥ 7.0, its methacrylic acid groups undergo rapid ionization, causing rapid dissolution of the coating layer.[38,39] This exposes the underlying chitosan core, which also swells in the alkaline environment. The combination of coating dissolution and core matrix erosion creates multiple pathways for drug diffusion and release.[40] The sustained release phase following the initial burst is consistent with Fickian diffusion from a swelling polymer matrix.[41]

The pronounced selectivity of the release system is quantitatively evident when comparing the release efficiency ratio between colonic and gastric conditions. At 24 hours, the colonic-to-gastric release ratio was 10.9 : 1 for PTX and 14.5 : 1 for SIM, demonstrating the strong pH-responsiveness of the system. This *in vitro* behavior confirms that the Eudragit S100–chitosan hybrid functions as a pH-triggered release platform, protecting the drug payload under acidic conditions and liberating it preferentially at higher pH. These results are mechanistically consistent with a rationale for preferential colonic drug exposure; however, they do not account for enzymatic degradation, mucus interactions, or absorption dynamics encountered *in vivo*. Therefore, *in vivo* pharmacokinetic and biodistribution studies are required to establish whether the pH-triggered release observed *in vitro* translates to actual site-specific colonic delivery under physiological conditions. In contrast to the pH-gated behavior of the nanoformulation, the free drug combination (Free PTX/SIM) exhibited rapid and essentially complete release under all three pH conditions, with no discriminatory barrier between the simulated GI compartments. Free PTX released 91.4 ± 3.2% and free SIM released 87.6 ± 3.5% of their respective doses within 8 hours at pH 1.2 (SGF), underscoring the vulnerability of unencapsulated drugs to premature gastric dissolution. Similarly, at pH 6.8 (SIF), cumulative release of free PTX and free SIM reached 94.2 ± 2.8% and 89.3 ± 3.1%, respectively, by 12 hours. At pH 7.4 (SCF), both free drugs demonstrated near-complete release (Free PTX: 96.5 ± 2.4%; free SIM: 92.1 ± 2.7%) within 6 hours. The absence of pH-selectivity in the free drug profiles confirms that without the protective nanocarrier architecture, both PTX and SIM would be subject to extensive absorption and first-pass metabolism in the upper GI tract before reaching the intended colonic site of action. These findings provide compelling quantitative evidence that nanoencapsulation within the Eudragit S100–chitosan hybrid system is essential for achieving the pH-triggered, preferential drug release in the colonic environment that underpins the therapeutic rationale of this formulation.

3.3.2. Mathematical modeling of release kinetics. To elucidate the underlying mechanisms governing drug release, the experimental release data from all three pH conditions were systematically fitted to four well-established mathematical models: zero-order, first-order, Higuchi, and Korsmeyer–Peppas equations (Table 4). Model discrimination was based primarily on the correlation coefficient (R^2).

For release in SGF, where drug liberation was severely restricted, the first-order model provided the best fit for both PTX ($R^2 = 0.9847$) and SIM ($R^2 = 0.9823$). The first-order kinetics suggest that the minimal drug release follows a diffusion-limited process through the intact, non-swelling polymer matrix.[42] The very low release rate constants reflect the formidable diffusion barrier. Alternative models, including zero-order and Higuchi, provided inferior fits.

In SIF, the Higuchi model emerged as the most appropriate descriptor for both drugs ($R^2 = 0.9882$ for PTX; $R^2 = 0.9865$ for SIM). The Higuchi equation describes drug release proportional to the square root of time and is characteristic of diffusion-controlled release from matrix systems.[43–45] The applicability of this model indicates that drug release proceeds primarily *via* Fickian diffusion through an increasingly hydrated but still structurally coherent polymer matrix. The Korsmeyer–Peppas model also provided good fits with release exponents (n) of 0.51 for PTX and 0.48 for SIM, values approaching 0.5 which further support a diffusion-dominated mechanism.[46,47]

The most complex release kinetics were observed in SCF, where the Korsmeyer–Peppas power law model provided superior fits ($R^2 = 0.9924$ for PTX; $R^2 = 0.9911$ for SIM). The calculated release exponents were $n = 0.73$ for PTX and $n = 0.69$ for SIM, both falling within the range of $0.5 < n < 1.0$, which is diagnostic of anomalous (non-Fickian) transport mechanisms.[48,49] These intermediate exponent values indicate that drug release at colonic pH involves a complex interplay of multiple simultaneous processes: polymer dissolution

(erosion), matrix swelling, and drug diffusion, all occurring concurrently at comparable rates.[50] The initial rapid release phase corresponds predominantly to Eudragit S100 coating dissolution and surface drug desorption, followed by a more gradual release phase driven by progressive chitosan chain relaxation and diffusion from the swelling gel network.[51]

The progressive shift in best-fit models from first-order (pH 1.2) to Higuchi (pH 6.8) to Korsmeyer–Peppas with anomalous exponents (pH 7.4) provides a kinetically coherent narrative of the pH-triggered transformation in release mechanisms, validating the formulation's sophisticated multi-modal responsiveness.[52,53] The zero-order model universally provided poor fits across all pH conditions, which is expected for matrix-based formulations.[54]

Kinetic analysis of the free PTX/SIM combination showed that drug release in all three media followed zero-order kinetics (R^2 > 0.98), indicating simple passive diffusion through the dialysis membrane without matrix-controlled resistance. No pH-dependent changes in the release model or exponent values were observed for the free drugs. In contrast, the nanoformulation exhibited a clear shift in release mechanism with increasing pH (first-order followed by Higuchi followed by Korsmeyer–Peppas anomalous transport), confirming that the complex, pH-responsive release behavior arises from the polymeric nanocarrier structure rather than the inherent physicochemical properties of the drugs. This distinction highlights the advantage of the nanoformulation in providing controlled, site-specific drug delivery that cannot be achieved with the free drug combination.

Overall, the comprehensive pH-dependent release characterization and mechanistic modeling confirm that the NP-PTX/SIM formulation exhibits the precise release characteristics required for a pH-responsive oral nanoformulation designed for preferential drug liberation in the colonic pH environment: gastric protection, intestinal retention, and pH-triggered drug release activation at neutral-to-alkaline pH. It is essential to note that these conclusions are based entirely on *in vitro* release data obtained in simplified buffer systems. *In vivo* pharmacokinetic and biodistribution studies will be required to verify whether these *in vitro* pH-triggered release characteristics translate into actual site-specific colonic delivery and therapeutic benefit *in vivo*.

3.3.3. Validation of release kinetics by orthogonal centrifugal ultrafiltration. To address the potential limitation of the dialysis bag method; namely, that drug–membrane interactions could lead to underestimation of release for lipophilic drugs such as simvastatin—the pH-dependent release behavior was reassessed using centrifugal ultrafiltration. This method directly separates nanoparticles from the release medium without an intervening dialysis membrane.

The cumulative release profiles obtained by ultrafiltration were in close agreement with the dialysis bag data for both PTX and SIM across all three pH conditions. The similarity between the two methods is quantified in Table S9, which presents the calculated similarity factor (f_2) values and the mean absolute differences in cumulative release at early (2 h) and late (24 h) time points. All f_2 values exceeded the commonly accepted threshold of 50 (range: 67.3–82.1), confirming good similarity. The mean absolute differences were ≤4.2% at 2 h and ≤1.5% at 24 h, indicating that any minor deviations observed, particularly a slightly faster release of simvastatin in SCF at early time points, do not alter the overall conclusion that the NP-PTX/SIM formulation exhibits minimal release in the upper GI tract and sustained, pH-triggered release in the colonic environment.

The free drug controls showed rapid and complete release (>95% within 6 h) with both methods, confirming that the ultrafiltration devices do not impede drug passage. The orthogonal study therefore validates the reliability of the dialysis-based release data and strengthens the evidence for the pH-responsive release capability of the Eudragit S100–chitosan hybrid nanoformulation, supporting its rational design as a platform for preferential drug liberation at colonic pH conditions *in vitro*.

3.4. Molecular docking analysis

Molecular docking analysis was performed to evaluate the binding affinities of simvastatin (CID 54454), pentoxifylline (CID 4740), and a representative monomer unit of Eudragit S100 against three target proteins: EGFR, CA9, and GSK3B as predicted from shared proteins extracted from Swiss target

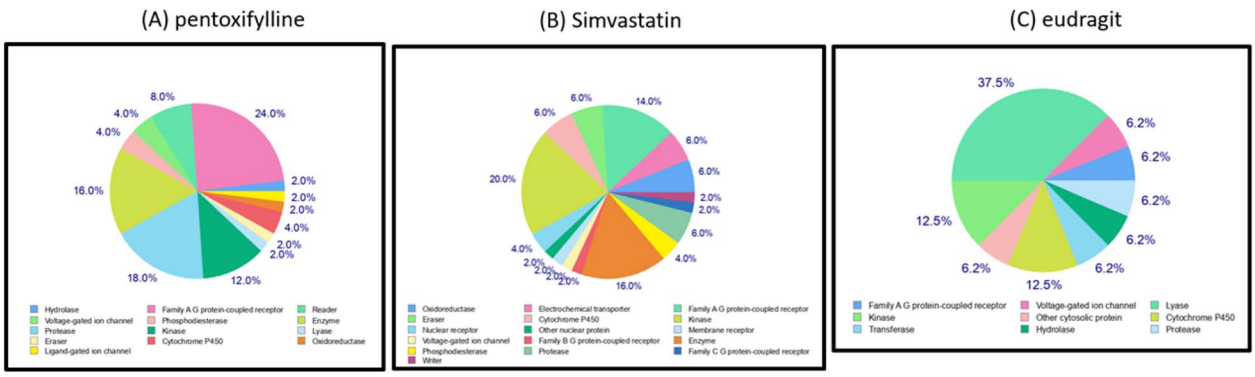

Fig. 8 (A–C) Pie chart visualization of target prediction of the three compounds; Pi chart visualizes the possible targets for our tested ligands, when some groups are shared between the three tested drug there are probable shared targets related to anti-cancer pathway.

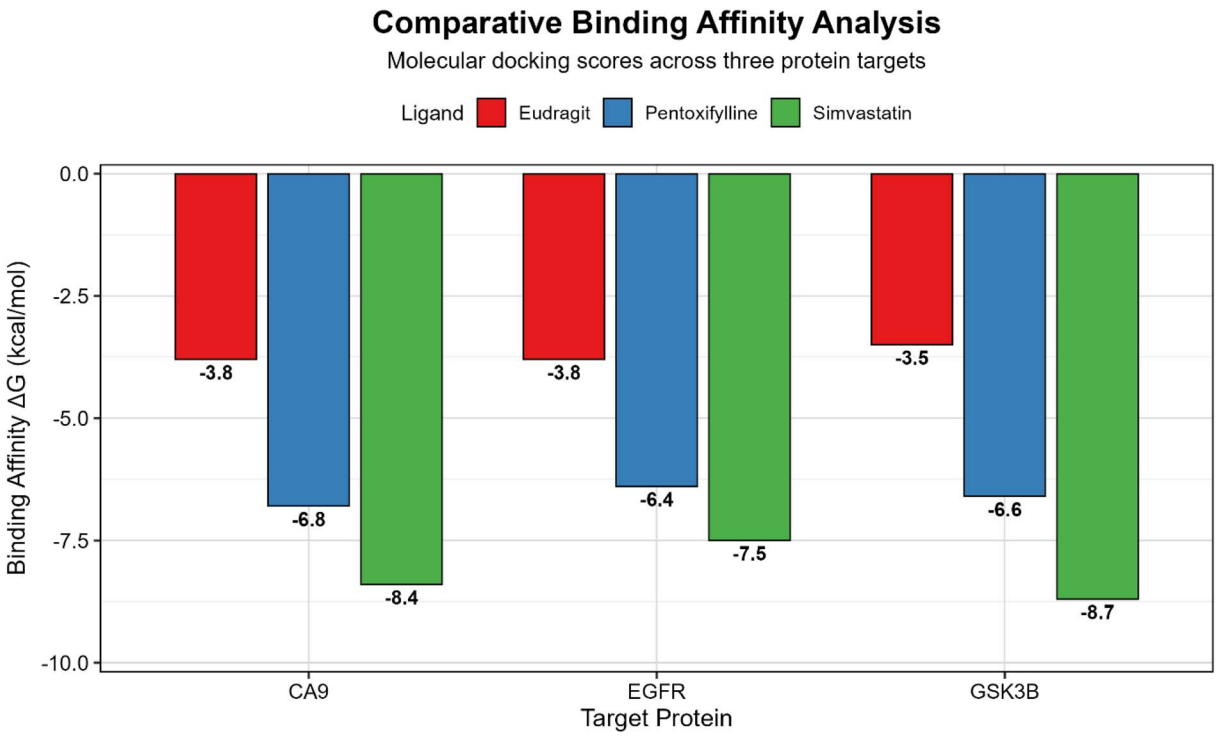

Fig. 9 Molecular docking binding affinity between the three ligands and proteins; figure represent the different in binding affinity between best suggested ligand simvastatin (green) and another candidate such pentoxifylline in blue and Eudragit in red bar, the most negative value represents the most binding favorability according to molecular docking analysis.

prediction shown in Fig. 8. The calculated binding free energies (ΔG, kcal mol^{-1}) are summarized in (Table 5) and summarized in Fig. 9 and provide insights into the relative interaction strengths and potential target preferences of the investigated ligands.

Overall, the molecular docking results indicated significant differences in binding affinities among the examined ligands, with simvastatin exhibiting the most favorable interactions with all three target proteins, scoring ΔG values of -7.5, -8.4, and -8.7 kcal mol^{-1} against EGFR, fold_ca9_q16790_200, and GSK3B, respectively. These results indicate a favorable and stable interaction profile, suggesting that simvastatin may possess a higher propensity to interact with these signaling-related proteins compared with the other tested compounds. Notably, the strongest interaction was observed with GSK3B, implying a potential inhibitory or modulatory role that may contribute to simvastatin's reported pleiotropic biological effects beyond its lipid-lowering activity. On the other hand, pentoxifylline demonstrated moderate binding affinities across all targets, with docking scores ranging from -6.4 to -6.8 kcal mol^{-1}. While, the Eudragit exhibited the weakest binding affinities toward all receptors, with ΔG values ranging from -3.5 to -3.8 kcal mol^{-1}.

As shown in Table 6, the RMSD values for simvastatin across all three targets ranged from 1.93 to 2.80 Å, with the GSK3β value (1.93 Å) falling below the 2.0 Å threshold for excellent reproducibility. Values for pentoxifylline similarly fell within acceptable limits (1.93–2.59 Å against GSK3β and EGFR, respectively).[55–57] These results confirm that both simvastatin and pentoxifylline reliably reproduced the crystallographic binding orientations, validating the robustness of the docking protocol for these primary investigational compounds. The

Table 6 RMSD validation of the molecular docking protocol. Values represent the average RMSD (Å) of the lower bound (L.B.) pose obtained by re-docking the native co-crystallized ligand into each protein binding site. RMSD <2.0 Å indicates excellent reproducibility, RMSD 2.0–3.0 Å indicates acceptable accuracy, and RMSD values approaching ~4.0 Å may be considered marginally acceptable for flexible ligands or induced-fit docking scenarios. RMSD values above ~4.0 Å, as observed for certain large or flexible ligands, indicate unreliable pose reproduction

Protein	Ligand	Average RMSD L.B. (Å)
EGFR (P00533)		
EGFR	Eudragit S100	3.99
EGFR	Pentoxifylline	2.34
EGFR	Simvastatin	2.80
CA9 (Q16790)		
CA9	Eudragit S100	2.98
CA9	Pentoxifylline	2.80
CA9	Simvastatin	2.72
GSK3β (P49841)		
GSK3β	Eudragit S100	6.15
GSK3β	Pentoxifylline	2.59
GSK3β	Simvastatin	1.93

RMSD values for Eudragit were notably higher, with EGFR (3.99 Å) and GSK3β (6.15 Å) exceeding conventional thresholds. While RMSD values approaching ~4.0 Å may be considered marginally acceptable for flexible ligands or induced-fit docking scenarios,[58] the GSK3β–Eudragit value (6.15 Å) clearly reflects unreliable pose reproduction. These elevated values likely result from Eudragit's large size, structural flexibility, and poor shape complementarity with the respective binding pockets, and should not be interpreted as indicative of protocol failure.

Overall, the RMSD validation demonstrates that the docking protocol is robust and reliable for simvastatin and pentoxifylline across all targets, whereas extreme RMSD values observed for Eudragit highlight limitations for large or structurally flexible ligands.

Data illustrated in (Table 7) show the interaction analysis for each of the predicted complexes. The simvastatin establishes several stabilizing interactions with EGFR as summarized in Fig. 10 and 11, including standard hydrogen bonds with SER1070 and THR1074 at distances of 2.71 Å and 3.26 Å, respectively. The hydrogen bonds are particularly important since serine and threonine residues in the EGFR kinase domain frequently participate in ATP binding and catalytic activity. Moreover, a carbon–hydrogen bond with PRO1073 at 3.09 Å, together with hydrophobic interactions with ALA920 and PRO1073, further fortify the ligand–protein complex.

The emergence of these various interaction types along with the robust binding affinity score suggest that simvastatin can efficiently occupy the EGFR active site, possibly disrupting the receptor's kinase function, resulting in inhibitory effects on receptor phosphorylation and downstream signaling pathways essential for tumor cell proliferation and survival. The interaction profile of simvastatin with CA9 as figured in Fig. 10 and 12 proved equally compelling, with the highest binding affinity among all tested combinations at −8.4 kcal mol^{-1}. Carbonic anhydrase IX is a transmembrane enzyme overexpressed in numerous solid tumors, where it regulates intracellular pH and facilitates tumor survival in hypoxic microenvironments. The strong binding affinity observed suggests that simvastatin may effectively target this enzyme, potentially disrupting the pH regulation mechanism that cancer cells exploit for survival and invasion. The molecular interaction analysis revealed conventional hydrogen bonds with TYR143 and ASN198 at distances of 2.77 Å and 2.97 Å respectively, both within optimal ranges for stable hydrogen bonding. Tyrosine and asparagine residues in the CA9 active site are known to participate in the catalytic mechanism and substrate coordination, suggesting that simvastatin binding in this region could interfere with enzymatic function. Furthermore, the pi-alkyl interaction with TRP141 at 4.69 Å provides additional stabilization through aromatic stacking interactions. This multifaceted binding pattern indicates that simvastatin can occupy the CA9 active site in a manner that may competitively inhibit its catalytic activity, thereby potentially compromising the ability of cancer cells to maintain favorable pH gradients necessary for their aggressive phenotype.

Simvastatin also exhibited remarkable binding affinity toward GSK3B with a score of −8.7 kcal mol^{-1}, the strongest binding observed in this study. Glycogen synthase kinase 3 beta plays a complex and context-dependent role in cancer, with aberrant GSK3B activity implicated in tumor progression, metastasis, and therapeutic resistance in various malignancies. The extensive network of interactions formed between simvastatin and GSK3B provides insights into the structural basis of this strong binding. The compound established four conventional hydrogen bonds with residues THR8, GLN89, ASN95, and ARG96, with distances ranging from 2.82 Å to 3.13 Å, all falling within the optimal range for hydrogen bonding. These residues are strategically located within the GSK3B ATP-binding pocket, suggesting that simvastatin may compete with ATP for binding to this kinase. Additionally, as summarized in Fig. 10 and figured in atomic details in Fig. 13; a carbon hydrogen bond with THR8 at 3.58 Å and hydrophobic interactions with VAL87 and PHE67 further enhance binding stability. The dual pi-alkyl interactions with PHE67 are particularly noteworthy, as phenylalanine residues in kinase binding pockets often contribute to selectivity and binding affinity through aromatic

Table 7 Interaction analysis of simvastatin with proteins

Target	Interaction	Distance	Category	Type
EGFR	A: SER1070:OG – A: simvastatin 1:O	2.70515	Hydrogen bond	Conventional hydrogen bond
EGFR	A: THR1074:OG1 – A: simvastatin 1:O	3.25707	Hydrogen bond	Conventional hydrogen bond
EGFR	A: PRO1073:CD – A: simvastatin 1:O	3.08586	Hydrogen bond	Carbon hydrogen bond
EGFR	A: ALA920 – A: simvastatin 1	4.36341	Hydrophobic	Alkyl
EGFR	A: PRO1073 – A: simvastatin 1	4.41716	Hydrophobic	Alkyl
CA9	A: TYR143:OH – A: simvastatin 1:O	2.77097	Hydrogen bond	Conventional hydrogen bond
CA9	A: ASN198:ND2 – A: simvastatin 1:O	2.97266	Hydrogen bond	Conventional hydrogen bond
CA9	A: TRP141 – A: simvastatin 1	4.68598	Hydrophobic	Pi-alkyl
GSK3B	A: THR8:OG1 – A: simvastatin 1:O	2.82368	Hydrogen bond	Conventional hydrogen bond
GSK3B	A: GLN89:NE2 – A: simvastatin 1:O	3.0355	Hydrogen bond	Conventional hydrogen bond
GSK3B	A: ASN95:ND2 – A: simvastatin 1:O	3.07721	Hydrogen bond	Conventional hydrogen bond
GSK3B	A: ARG96:N – A: simvastatin 1:O	3.12901	Hydrogen bond	Conventional hydrogen bond
GSK3B	A: simvastatin 1:C – A: THR8:OG1	3.58399	Hydrogen bond	Carbon hydrogen bond
GSK3B	A: VAL87 – A: simvastatin 1	4.77567	Hydrophobic	Alkyl
GSK3B	A: PHE67 – A: simvastatin 1	5.33817	Hydrophobic	Pi-alkyl
GSK3B	A: PHE67 – A: simvastatin 1	5.21435	Hydrophobic	Pi-alkyl

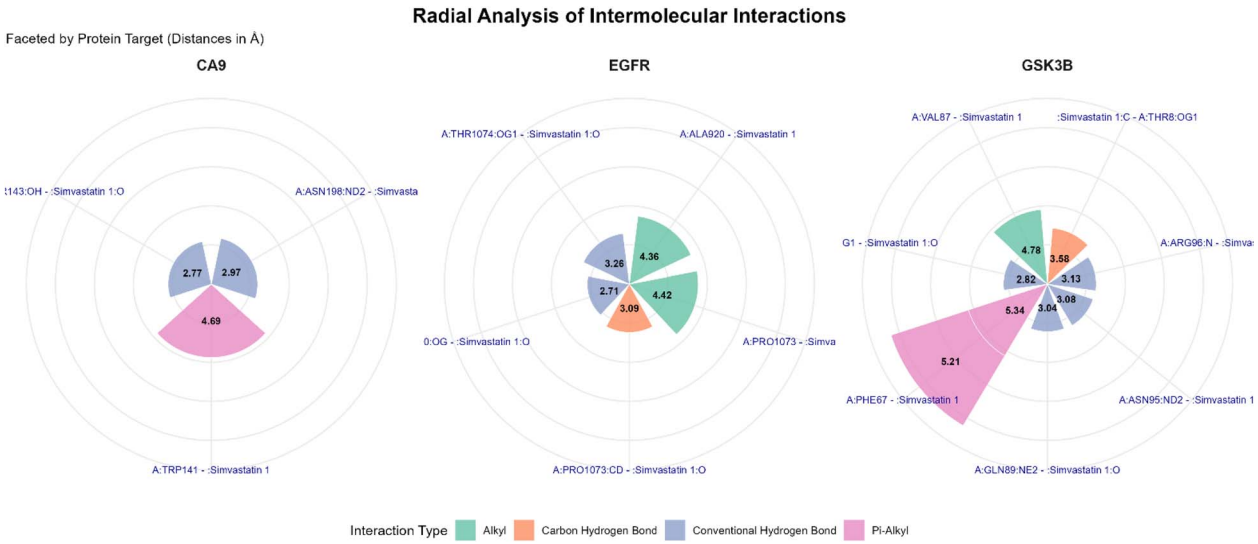

Fig. 10 Intermolecular interaction and atomic details between simvastatin and proteins; figure represent the summery of bond formation between best ligand candidate simvastatin and three proteins that shared in swiss target report between all three ligands, the blue color represent the presence of H-bond with relative short strong distance, and red color for pi-alkyl interaction while green color alkyl interaction, the orange color represent the C–H bond, that mention that drug have two properties hydrophobic (alkyl, pi-alkyl) and polar (H-bond, C–H bond) interactions.

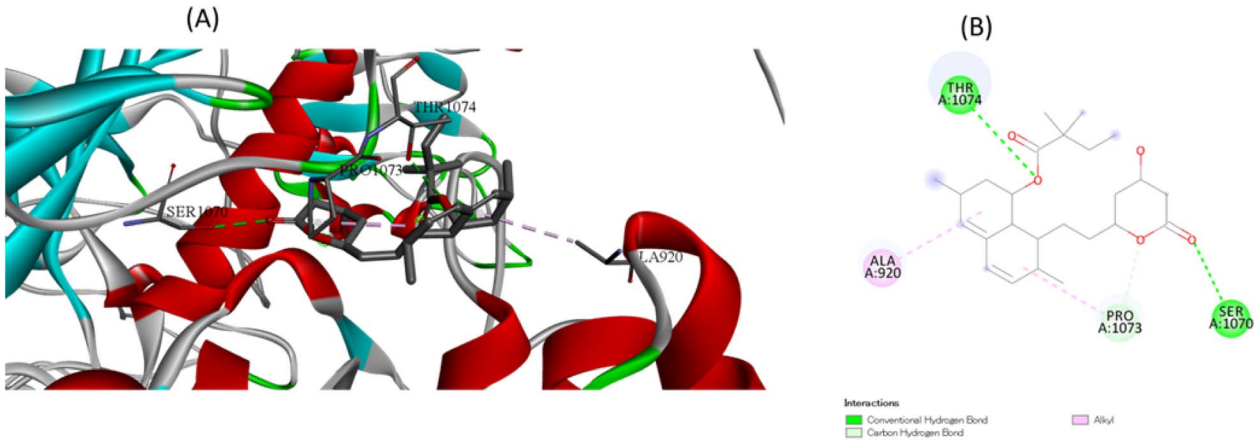

Fig. 11 3D (A) and 2D (B) interaction visualization between EGFR and simvastatin; 3D (A) visualization for interaction between our drug simvastatin and EGFR with red color for α-helix and blue color for B-sheet and 2D interaction (B) represent that drug have polar criteria to form H-bond in addition to hydrophobic ability to form alkyl bonds.

interactions. This comprehensive interaction profile suggests that simvastatin can effectively occupy the GSK3B active site, potentially modulating the kinase activity that influences multiple cancer-relevant pathways including cell survival, proliferation, and metabolic regulation.

The consistently poor performance of Eudragit across all three targets, with binding affinities ranging from −3.5 to −3.8 kcal mol^{-1}, suggests limited therapeutic potential for direct interaction with these cancer-related proteins. These weak binding affinities likely reflect insufficient complementarity between Eudragit's chemical structure and the binding pockets of the target proteins. Pentoxifylline demonstrated intermediate binding affinities ranging from −6.4 to −6.8 kcal mol^{-1}, indicating moderate potential for interaction with these targets. While pentoxifylline showed reasonable binding capabilities, its interactions were not characterized in detail in this study, leaving questions about the specific molecular contacts that stabilize these complexes. Nevertheless, the observed binding affinities suggest that pentoxifylline may warrant further investigation as a potential adjuvant therapy, particularly given its established safety profile and anti-inflammatory properties that could complement anti-cancer strategies.

The findings of this study contribute significantly to bridging the gap between computational prediction and therapeutic repurposing of established drugs. Simvastatin, primarily

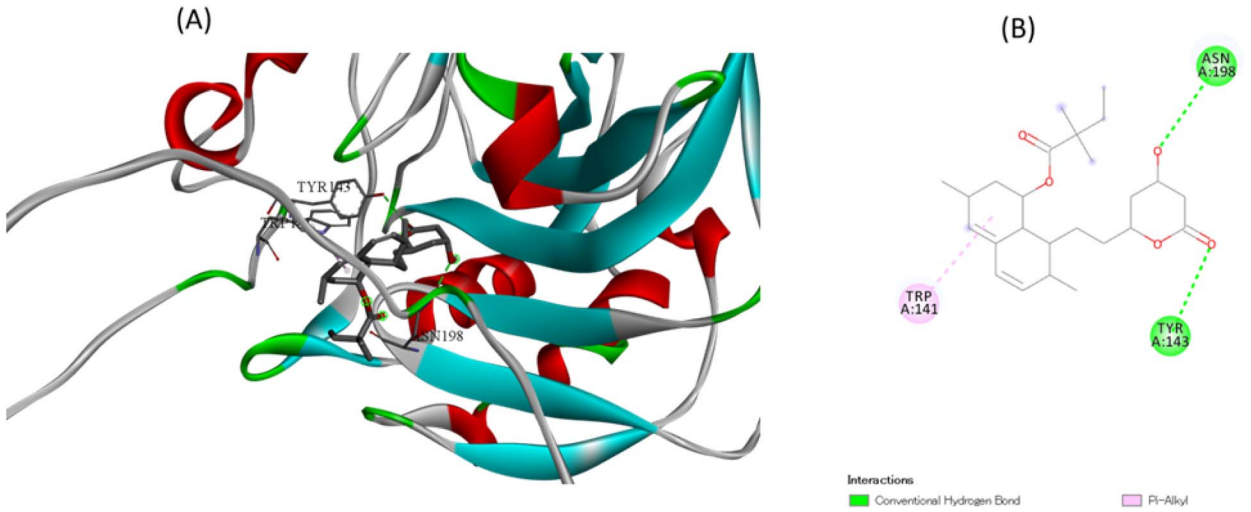

Fig. 12 3D (A) and 2D (B) interaction visualization between CA9 and simvastatin; 3D (A) visualization for interaction between our drug simvastatin and CA9 with red color for α-helix and blue color for B-sheet and 2D interaction (B) represent that drug have polar criteria to form H-bond in addition to hydrophobic ability to form alkyl bonds.

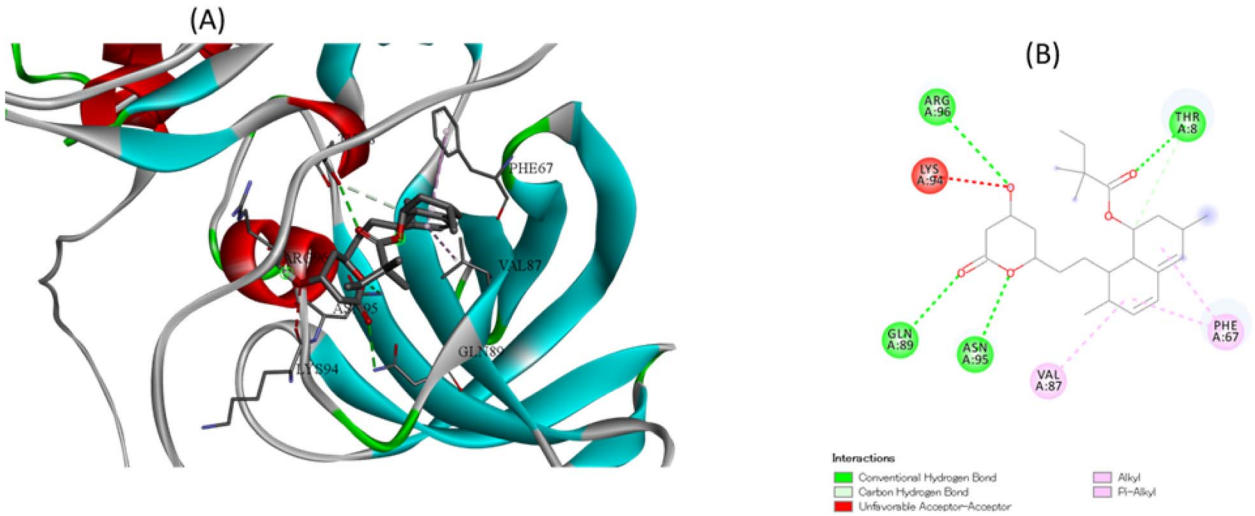

Fig. 13 3D (A) and 2D (B) interaction visualization between GSK3B and simvastatin; 3D (A) visualization for interaction between our drug simvastatin and GSK3B with red color for α-helix and blue color for B-sheet and 2D interaction (B) represent that drug have polar criteria to form H-bond in addition to hydrophobic ability to form alkyl bonds when show more H-bond formation capability from compound left side more than rest of proteins.

prescribed as a lipid-lowering agent, has garnered increasing attention for its potential pleiotropic effects in cancer prevention and treatment. Epidemiological studies have suggested associations between statin use and reduced cancer risk or improved outcomes in certain malignancies, though the mechanisms underlying these observations have remained incompletely understood. The present study provides molecular-level evidence that simvastatin can directly interact with key oncogenic proteins through favorable binding interactions. The strong binding affinities observed, particularly the -8.7 kcal mol^{-1} interaction with GSK3B and -8.4 kcal mol^{-1} with CA9, are comparable to or exceed those of many known inhibitors, suggesting genuine potential for therapeutic activity. The detailed interaction profiles reveal that simvastatin engages these targets through networks of hydrogen bonds and hydrophobic contacts that span critical functional residues, providing a structural rationale for potential inhibitory activity.

These computational findings align with and extend previous research exploring the anti-cancer properties of statins. Multiple preclinical studies have demonstrated that statins can inhibit cancer cell proliferation, induce apoptosis, and suppress metastasis through mechanisms that extend beyond cholesterol biosynthesis inhibition. The current study provides a mechanistic framework suggesting that direct binding to cancer-relevant protein targets may contribute to these observed effects. The ability of simvastatin to interact favorably

with EGFR, CA9, and GSK3B simultaneously suggests potential for polypharmacology, where a single agent modulates multiple disease-relevant targets. This characteristic could be particularly advantageous in cancer therapy, where tumors often exhibit redundancy in oncogenic signaling pathways and develop resistance through compensatory mechanisms when single targets are inhibited.

The interaction data also illuminate how molecular recognition drives biological activity in the context of protein–ligand binding. The predominance of hydrogen bonding interactions in the simvastatin complexes reflects the importance of electrostatic complementarity in achieving high-affinity binding. Hydrogen bonds provide both specificity and strength to molecular recognition, with the optimal distances observed in this study indicating well-matched donor–acceptor geometries. The supplementary hydrophobic interactions contribute entropic stabilization by excluding water molecules from the binding interface and providing van der Waals contacts that enhance overall binding affinity. For kinases like EGFR and GSK3B, the positioning of simvastatin interactions within ATP-binding regions suggests a competitive inhibition mechanism, where the ligand occupies space normally reserved for the natural substrate. For CA9, interactions near catalytic residues imply potential for active site blockade, which would impair the enzyme's ability to catalyze the conversion of carbon dioxide to bicarbonate and protons.

The convergence of computational predictions with biological plausibility strengthens the translational potential of these findings. The binding affinities predicted through docking simulations provide quantitative estimates of interaction strength that can inform prioritization for experimental validation. Typically, binding affinities more negative than -6.0 kcal mol^{-1} are considered indicative of meaningful interactions worthy of further investigation, and simvastatin exceeded this threshold against all three targets. Moreover, the consistency of simvastatin's superior performance across structurally and functionally distinct proteins enhances confidence in the robustness of these predictions. While computational docking provides valuable initial insights, it represents only the first step in drug discovery and repurposing pipelines. Experimental validation through biochemical assays, cellular studies, and ultimately clinical investigation will be essential to confirm these computational predictions and translate them into therapeutic applications.

This study completes an important piece of the puzzle in understanding how established drugs might be repurposed for cancer treatment based on molecular interactions with validated oncogenic targets. By systematically evaluating binding affinities and characterizing interaction patterns, we have identified simvastatin as a promising candidate for further development as a multi-target anti-cancer agent. The molecular insights gained from interaction analysis provide testable hypotheses about mechanisms of action and guide the design of subsequent experimental studies. Furthermore, these findings exemplify the power of computational approaches in accelerating drug discovery by enabling rapid, cost-effective screening of compound libraries against multiple therapeutic targets before committing resources to extensive experimental campaigns.

3.5. Anti-proliferative cytotoxic effects (anti-cancer activity)

The maximal anti-proliferative effects were observed in HCT-116 cells following treatment with the NP-PTX/SIM formulation followed by SIM and PTX. The anti-cancerous effect of the tested substances was concentration dependent in which the cytotoxic inhibitory effects increased with increasing the concentration as shown in Fig. 14. Fig. 15 confirmed the previous observation in which the IC_{50} reached about (10.21 μg mL^{-1}, 53.61 μg mL^{-1}, and 91.99 μg mL^{-1}) for NP-PTX/SIM, free simvastatin, and pentoxifylline respectively.

3.5.1. Morphological changes. Fig. 16 showed intact cellular sheet of purple-stained adherent monolayers of polygonal or rounded shaped HCT116 cells, which are tightly closed together forming well defined colonies. Upon treatment with the tested substances, cells undergo apoptosis and became more shrunken with development of cytoplasmic vacuoles and pyknotic nuclei subsequently they lose their adherence with detachment of the cellular sheet. The cytotoxic apoptotic effects were increased with increasing the concentration and more obvious in cells treated with NP-PTX/SIM. The high percentage of the detached cells was observed at the high concentrations of NP-PTX/SIM followed by SIM and PTX.

To formally establish the nature of the pharmacological interaction between PTX and SIM in the co-delivery system, the CI was determined using the Chou–Talalay method as described in Section 2.7.4. Based on the IC_{50} values of free PTX (91.99 μg mL^{-1}), free SIM (53.61 μg mL^{-1}), and NP-PTX/SIM (10.21 μg mL^{-1}), and the fixed PTX-to-SIM mass ratio of 13.3 : 1 in the nanoformulation, the calculated CI at the IC_{50} effect level was CI = 0.42. According to established Chou–Talalay criteria, a CI value in the range of 0.3–0.7 is classified as *synergism*. A CI of 0.42 therefore confirms a strong synergistic interaction between PTX and SIM when co-encapsulated and co-delivered as NP-PTX/SIM to HCT-116 colorectal cancer cells. This synergy is mechanistically consistent with the complementary and convergent anti-cancer pharmacology of the two drugs: SIM disrupts the mevalonate/Ras/PI3K pro-survival axis, while PTX simultaneously dismantles the NF-κB/TNF-α inflammatory survival programme, producing a combined pro-apoptotic stimulus that is substantially greater than the sum of individual contributions.

It should be noted that the CI analysis was performed exclusively in HCT-116 cells, which represent a well-characterized p53 wild-type, KRAS-mutant colorectal cancer model. Validation of this synergistic interaction in additional CRC cell lines with distinct molecular profiles (*e.g.*, HT-29: BRAF-mutant, p53-mutant; SW480: KRAS-mutant, p53-mutant) is recognized as an important future direction to establish the generalizability of this finding across the molecular heterogeneity of colorectal cancer.

Induction of apoptosis and oxidative stress are the main mechanisms for the anti-proliferative effect of simvastatin against HCT116, moreover it has the ability to induce pyroptosis

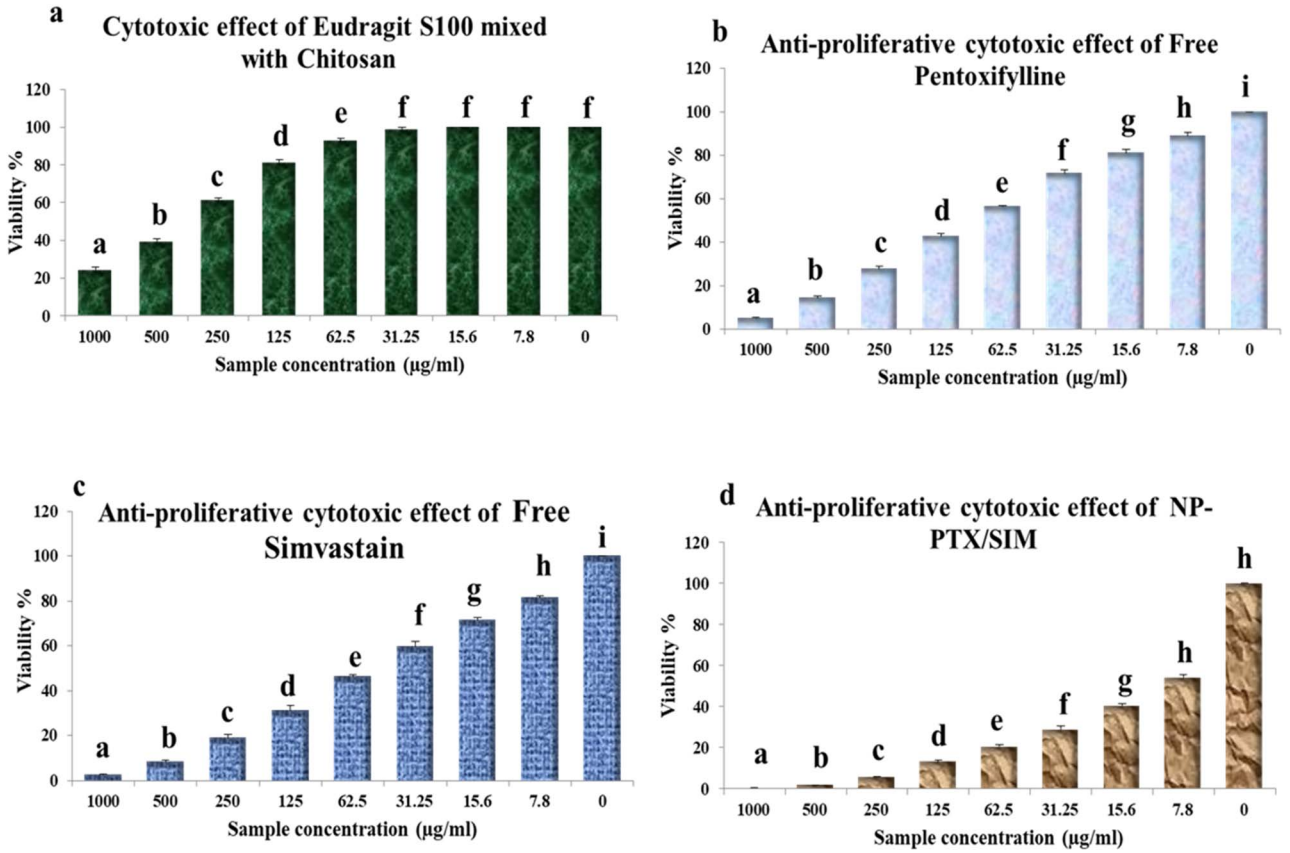

Fig. 14 (a–d) Anti-proliferative cytotoxic effect of the tested substances (a) Eudragit S100 mixed with chitosan, (b) free pentoxifylline, (c) free simvastatin, and (d) NP-PTX/SIM against HCT-116 cell line at various concentrations.

through activation of ROS/caspase-1/GSDMD signaling pathway.[59] Liu *et al.* (2020) linked the apoptotic effect of simvastatin to its ability to inhibit the β-catenin and yes-associated protein (YAP) through the GGPP-dependent pathway.[60]

The apoptotic effect of PTX was reported to be the main mechanism for its anti-proliferative effects against variable tumor cell lines.[61,62] Al-Husein *et al.* explained that the apoptotic effect of PTX against colorectal cancer cell lines is cell line dependent, as it produced more apoptotic effect against SW480 cells than HCT-116 cells; furthermore, its apoptotic effect was caspase-dependent and mediated *via* the mitochondria.[10]

PTX was reported to have synergistic effect with other chemotherapeutic agents as documented in the previous studies beside its capability to suppress the cell viability.[63,64] This synergistic effect with the anti-cancerous therapies may be attributed to its ability to suppress the matrix metalloproteinases and P-glycoprotein 65. This effect was documented clearly in the present study, in which the anti-proliferative cytotoxic effects of NP-SIM/PTX begun at very low concentration (7.8 µg mL^{-1}) and resulted in the maximal anti-cancerous activity at very low concentration (10.21 µg mL^{-1}) in comparison to free forms of both. The cytotoxic apoptotic effect of the nanoformulated combination was identified clearly in the cellular morphology of HCT-116 that representing in extensively shrunken cells with cytoplasmic vacuoles and pyknotic nuclei.

3.6. Assessment of apoptotic and proliferative biomarkers

The illustrated results in Fig. 17a–c, revealed a consistent and statistically significant hierarchy across all three biomarkers, with NP-PTX/SIM producing the greatest caspase-3 activation, the most pronounced Ki-67 suppression, and the lowest VEGF secretion of all treatment groups ($p < 0.001$ *vs.* free SIM, free PTX, and Eudragit S100 mixed with chitosan for all endpoints), establishing that the nanoformulation induces genuine multi-mechanistic programmed cell death rather than passive cytostasis at its remarkably low therapeutic IC_{50}.

3.6.1. Carrier biocompatibility. Eudragit S100 mixed with chitosan treatment produced no statistically significant alteration in caspase-3 activity (1.19 ± 0.11 nmol pNA per mg protein per h; Fig. 17a), Ki-67 expression (831.6 ± 28.9 pg mL; Fig. 17b), or VEGF secretion (308.5 ± 21.2 pg mL^{-1}; Fig. 17c) relative to untreated control cells (1.12 ± 0.09 nmol pNA per mg protein per h; 847.4 ± 31.6 pg mL^{-1}; 312.8 ± 18.4 pg mL^{-1}, respectively; all $p > 0.05$). These findings are fully consistent with the Eudragit S100 mixed with chitosan IC_{50} of 379.50 µg mL^{-1} recorded in the MTT assay, a value 37.2-fold greater than the therapeutic IC_{50} of NP-PTX/SIM, and confirm that the Eudragit S100–chitosan carrier exerts no intrinsic cytotoxic, anti-

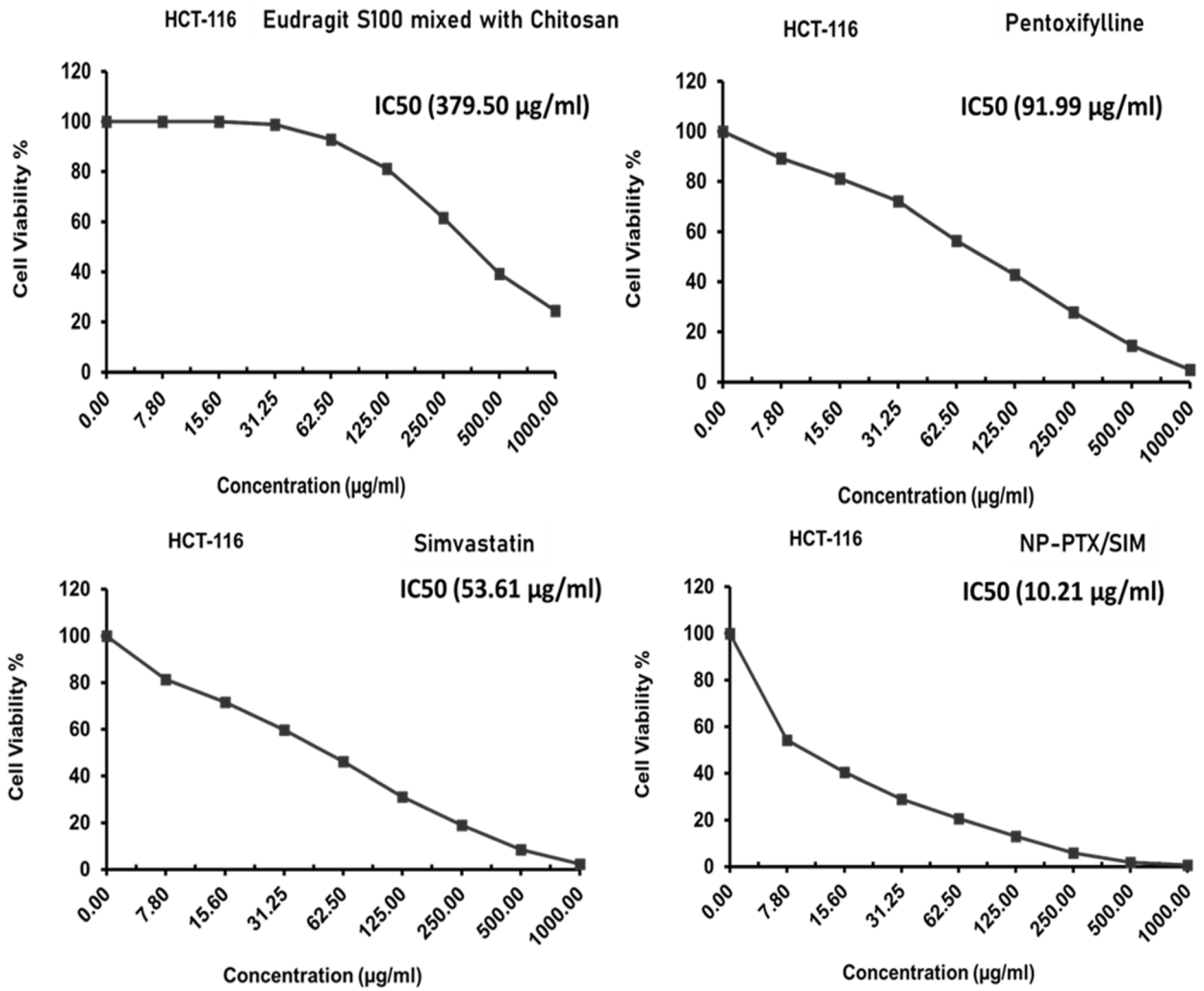

Fig. 15 IC_{50} values of the tested substances (Eudragit S100 mixed with chitosan, free pentoxifylline, free simvastatin, and NP-PTX/SIM) against HCT-116 cell line.

proliferative, or anti-angiogenic influence at pharmacologically relevant concentrations. The totality of biological activity observed with the drug-loaded formulation is therefore unambiguously attributable to the co-encapsulated PTX and SIM, validating the biocompatibility of the polymer carrier system, consistent with the well-established safety profiles of chitosan and Eudragit S100 as pharmaceutical excipients.[13,33]

3.6.2. Caspase-3 activation and apoptotic induction. NP-PTX/SIM elicited the highest caspase-3 activity of all treatment groups (5.64 ± 0.27 nmol pNA per mg protein per h; Fig. 17a), representing a 5.03-fold increase over Eudragit S100 mixed with chitosan, a 2.81-fold increase over free PTX (2.01 ± 0.08 nmol pNA per mg protein per h), and a 2.30-fold increase over free SIM (2.45 ± 0.10 nmol pNA per mg protein per h; $p < 0.001$ for all comparisons), despite being administered at a 9.01- and 5.25-fold lower molar dose than free PTX and free SIM, respectively. Notably, free SIM produced significantly greater caspase-3 activation than free PTX ($p < 0.05$; Fig. 17a), consistent with simvastatin's direct inhibition of the mevalonate pathway and its stronger docking-predicted engagement with GSK3β ($\Delta G = -8.7$ kcal mol^{-1}, Section 3.3). This disproportionate caspase-3 induction by NP-PTX/SIM at a sub-11 µg mL^{-1} IC_{50} establishes that nanoencapsulation and co-delivery substantially amplify the apoptotic potency of the drug combination beyond what either agent achieves independently at their respective free-drug IC_{50} doses.

The mechanistic basis of this activation is rooted in the complementary pro-apoptotic pharmacology of both encapsulated agents. Simvastatin inhibits the mevalonate pathway, depleting cells of the isoprenoid intermediates required for Ras and Rho GTPase prenylation, thereby disrupting PI3K/Akt and MAPK pro-survival signaling and disinhibiting the intrinsic mitochondrial apoptotic cascade.[6,7] This mechanism is directly reinforced by the molecular docking results of Section 3.3, where simvastatin demonstrated the highest binding affinity of all tested ligands against GSK3β ($\Delta G = -8.7$ kcal mol^{-1}). Active GSK3β promotes phosphorylation and proteasomal degradation of the anti-apoptotic protein MCL-1 while activating the

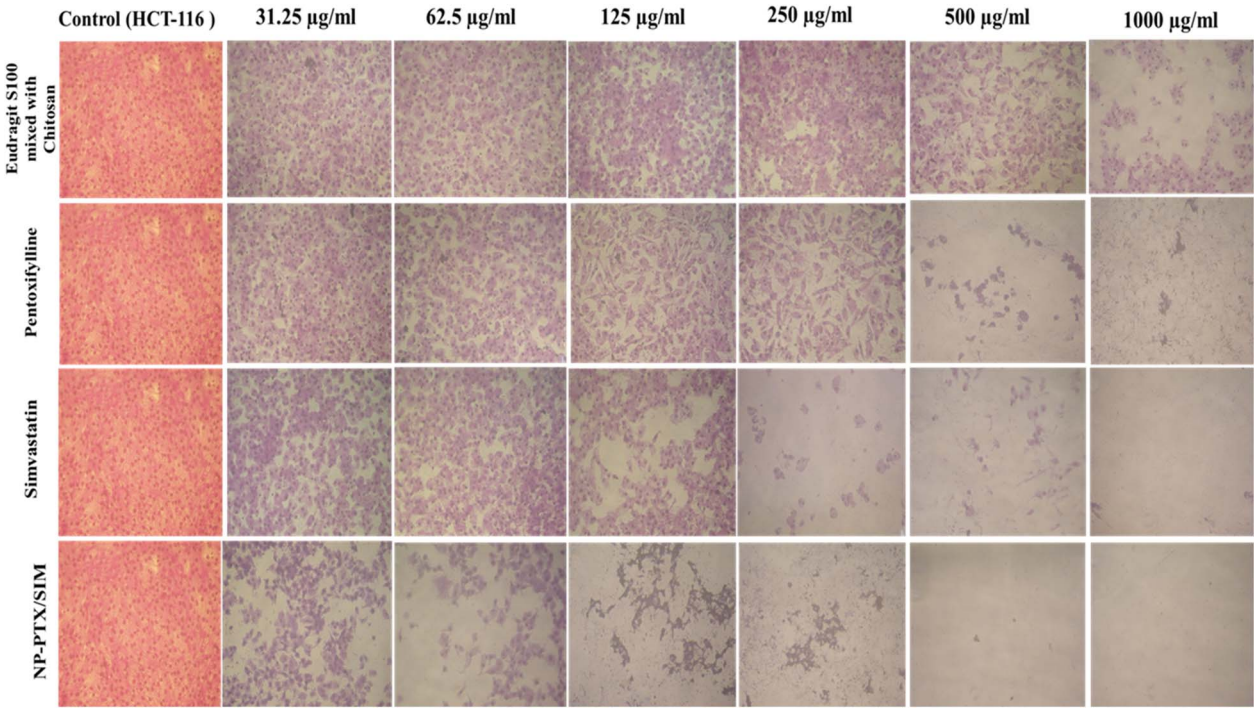

Fig. 16 Morphological changes of HCT-116 cell line following treatment with Eudragit S100 mixed with chitosan, free pentoxifylline, free simvastatin, and (NP-PTX/SIM) at different concentrations. (Crystal violet, 200×).

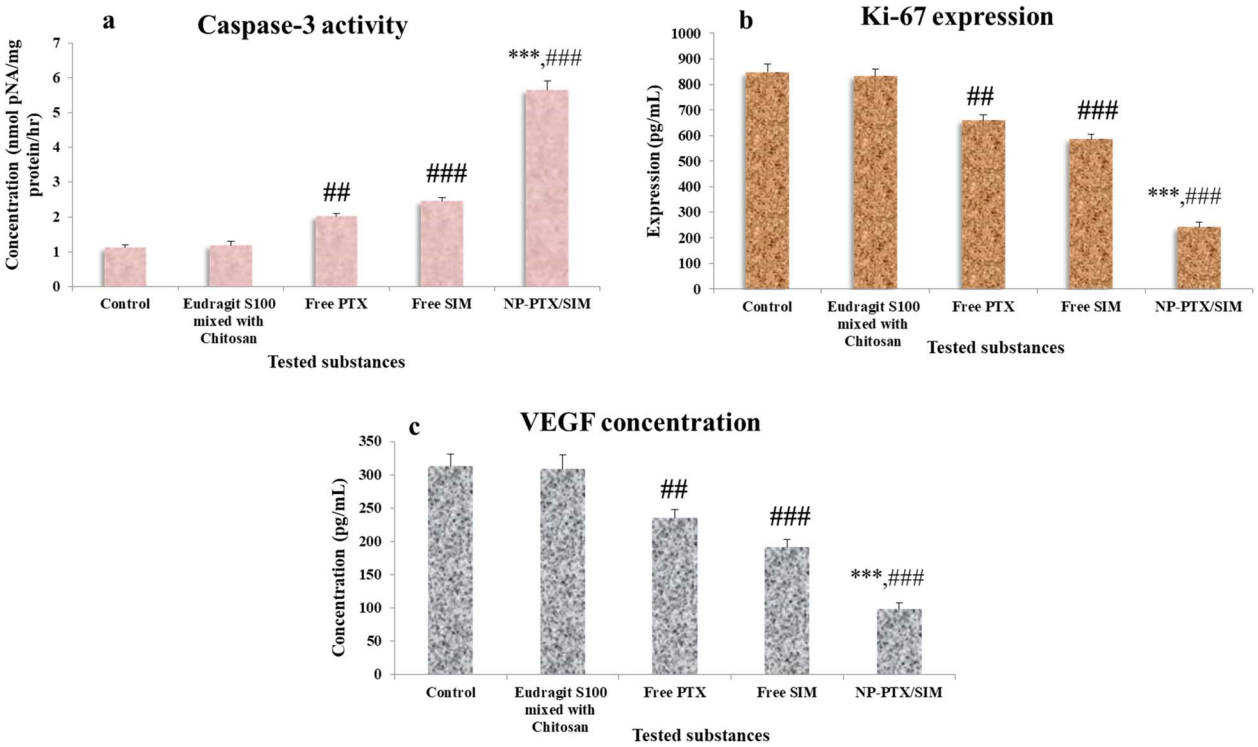

Fig. 17 Effects of NP-PTX/SIM on apoptotic, proliferative, and angiogenic biomarkers in HCT-116 colorectal cancer cells. (a) Caspase-3 activity, (b) Ki-67 expression, and (c) VEGF secretion following treatment with NP-PTX/SIM, free PTX, free SIM, and blank Eudragit S100–chitosan nanoparticles. NP-PTX/SIM significantly increased caspase-3 activity while markedly decreasing Ki-67 and VEGF levels compared with free drugs and carrier control ($p < 0.001$), indicating enhanced pro-apoptotic, anti-proliferative, and anti-angiogenic effects. The blank carrier showed no significant changes *versus* untreated cells ($p > 0.05$), confirming its biocompatibility. Data are presented as mean ± SD.

pro-apoptotic BH3-only sensitizer BIM, converging on mitochondrial outer membrane permeabilization, cytochrome c release, and downstream caspase-3 cleavage.[7] The measured caspase-3 elevation (Fig. 17a) thus provides direct *in vitro* functional validation of the computationally predicted simvastatin–GSK3β interaction, establishing a coherent mechanistic bridge between the *in silico* findings of Section 3.3 and the cellular biological outcomes reported here. Pentoxifylline augments this apoptotic program through inhibition of NF-κB transcriptional activity and TNF-α production, dismantling the NF-κB-driven expression of Bcl-2, Bcl-xL, survivin, and XIAP that otherwise suppress caspase activation.[9–11] The concurrent removal of NF-κB-mediated anti-apoptotic gene expression by PTX and Ras/PI3K/Akt survival signaling by SIM produces a convergent and amplified pro-apoptotic stimulus that is mechanistically consistent with the strong synergistic Combination Index of 0.42 established in the cytotoxicity assay, and concordant with the reported synergistic pro-apoptotic effects of this drug pair.[12]

The superiority of NP-PTX/SIM over both free drugs in caspase-3 induction at dramatically lower molar doses is principally attributable to the nanocarrier-mediated intracellular delivery advantage. Endocytic nanoparticle internalization bypasses P-glycoprotein and MRP efflux transporters overexpressed in HCT-116 cells, achieving higher intracellular drug concentrations per unit nominal dose.[4,5] The positive surface charge of +31.2 ± 1.5 mV facilitates electrostatic-driven membrane adsorption and endocytic uptake,[13,14] while the sustained anomalous (non-Fickian) intracellular release kinetics established in Section 3.2 maintain pro-apoptotic drug levels within the cell over an extended duration, perpetuating caspase-3 activation beyond the transient exposure achievable with either free drug alone.

3.6.3. Ki-67 suppression and anti-proliferative activity. NP-PTX/SIM reduced Ki-67 expression to 241.7 ± 19.3 pg mL^{-1} (Fig. 17b), representing a 70.9% suppression relative to blank nanoparticle controls (831.6 ± 28.9 pg mL^{-1}; $p < 0.001$). This was significantly greater than the 20.7% Ki-67 reduction achieved by free PTX (659.5 ± 21.4 pg mL^{-1}; $p < 0.001$ *vs.* NP-PTX/SIM) and the 29.6% reduction by free SIM (585.2 ± 18.7 pg mL^{-1}; $p < 0.001$ *vs.* NP-PTX/SIM; Fig. 17b). The significantly greater Ki-67 suppression by free SIM compared to free PTX ($p < 0.05$; Fig. 17b) reflects simvastatin's dual inhibitory action on both Ras/MAPK and Wnt/β-catenin proliferative axes, while pentoxifylline's anti-proliferative effect operates primarily through cAMP/PKA-mediated Raf-1 inactivation.[7] Together in the nanoformulation, these complementary mechanisms converge to produce a 70.9% Ki-67 suppression at the remarkably low IC_{50} of 10.21 μg mL^{-1}, substantially exceeding what either agent achieves individually at higher free-drug doses.

Ki-67 expression is co-regulated by multiple proliferative signaling axes directly and convergently targeted by both encapsulated agents. Simvastatin's blockade of Ras prenylation suppresses the Ras/RAF/MEK/ERK mitogenic cascade, reducing transcriptional activation of Ki-67 and its downstream cell cycle effectors cyclin D1, CDK4, and c-Myc.[7] Additionally, the high-affinity simvastatin–GSK3β interaction ($\Delta G = -8.7$ kcal mol^{-1}, Section 3.3) introduces a second orthogonal anti-proliferative mechanism through GSK3β-mediated β-catenin phosphorylation and proteasomal degradation, suppressing Wnt/β-catenin-driven transcription of Ki-67 and cyclin D1 independently of mevalonate effects.[11] Pentoxifylline contributes through phosphodiesterase inhibition, elevating intracellular cAMP and activating PKA, which phosphorylates and inactivates Raf-1, a critical convergence points on the MAPK proliferative axis. The simultaneous suppression of Ras/MAPK, Wnt/β-catenin, and cAMP/PKA-Raf proliferative programs by PTX and SIM acting together in the nanoformulation accounts for the 70.9% Ki-67 reduction at the low NP-PTX/SIM IC_{50} dose (Fig. 17b). Given that persistent Ki-67 suppression in residual CRC tumor cells is an established predictor of reduced recurrence and improved disease-free survival,[7,8] this finding suggests that NP-PTX/SIM may confer durable anti-tumor benefits extending beyond the immediate cytotoxic response.

3.6.4. VEGF down regulation and anti-angiogenic activity. NP-PTX/SIM produced the most potent suppression of VEGF secretion among all groups (98.2 ± 9.7 pg mL^{-1}; Fig. 17c), representing a 68.2% reduction relative to Eudragit S100 mixed with chitosan controls (308.5 ± 21.2 pg mL^{-1}; $p < 0.001$), a 58.1% reduction compared to free PTX (234.6 ± 13.2 pg mL^{-1}; $p < 0.001$), and a 48.7% reduction compared to free SIM (191.4 ± 11.8 pg mL^{-1}; $p < 0.001$; Fig. 17c). Free SIM produced significantly greater VEGF suppression than free PTX ($p < 0.05$; Fig. 17c), consistent with simvastatin's dual HIF-1α/CA9-mediated anti-angiogenic mechanism, which is mechanistically richer than pentoxifylline's NF-κB/TNF-α-mediated pathway alone. The NP-PTX/SIM formulation surpassed both individual free drug responses at a fraction of their molar doses, establishing that nanoencapsulated co-delivery produces a synergistic anti-angiogenic outcome that neither agent achieves independently.

Simvastatin suppresses VEGF transcription through two convergent mechanisms supported by both pharmacological and computational evidence. First, mevalonate pathway inhibition reduces constitutive HIF-1α activation, the principal transcriptional activator of VEGF under the hypoxic conditions that characterize the CRC tumor microenvironment.[6,7] Second, the molecular docking data of Section 3.3 demonstrated that simvastatin binds CA9 with high affinity ($\Delta G = -8.4$ kcal mol^{-1}) through conventional hydrogen bonds with TYR143 and ASN198 and a stabilizing pi-alkyl interaction with TRP141. CA9 sustains the intracellular alkalinity stabilizing HIF-1α against proteasomal degradation in hypoxic conditions; its inhibition suppresses VEGF transcription through a mechanism independent of and additive to Ras/HIF-1α suppression.[8] The measured VEGF reduction by free SIM and its further amplification in NP-PTX/SIM (Fig. 17c) therefore provides functional *in vitro* corroboration of the computationally predicted CA9 inhibition, directly connecting the docking findings of Section 3.3 to the cellular anti-angiogenic outcomes reported here. Pentoxifylline contributes complementarily through NF-κB and TNF-α inhibition, dismantling a major transcriptional inducer of VEGF in CRC cells.[9,10] The concurrent suppression of the HIF-1α/CA9 angiogenic axis by SIM and the NF-κB/TNF-α pro-

angiogenic inflammatory axis by PTX within the same nanocarrier produces a convergent and complementary VEGF reduction consistent with the synergistic CI of 0.42. The clinical significance of the 68.2% VEGF reduction achieved at the low IC_{50} of 10.21 μg mL^{-1} is considerable: VEGF drives not only primary tumor neovascularization but also vascular permeability and haematogenous metastatic dissemination in advanced CRC,[2,8] and its suppression to near-residual levels portends reduced metastatic potential alongside the direct antitumor cytotoxicity established in the MTT assay.

3.6.5. Integrative mechanistic interpretation. Taken together, the caspase-3 (Fig. 17A), Ki-67 (Fig. 17B), and VEGF (Fig. 17C) data reveal a mechanistically unified, three-dimensional anticancer pharmacology for NP-PTX/SIM that is directly grounded in and fully consistent with every preceding section of this manuscript. Across all three biomarker endpoints, the response hierarchy was consistent: NP-PTX/SIM ≫ free SIM > free PTX > blank NPs ≈ untreated control, reflecting the additive-to-synergistic pharmacological interaction between co-delivered PTX and SIM and the amplifying effect of nanoparticle-mediated intracellular delivery. The GSK3β binding affinity ($\Delta G = -8.7$ kcal mol^{-1}, Section 3.3) is functionally reflected in both caspase-3 activation and Ki-67 suppression; the CA9 binding affinity ($\Delta G = -8.4$ kcal mol^{-1}, Section 3.3) is functionally reflected in VEGF suppression; and the synergistic CI of 0.42 (determined by the Chou–Talalay method in HCT-116 cells, Section 3.4) is mechanistically grounded in the convergent multi-pathway modulation by PTX and SIM across all three biomarker axes simultaneously. The consistent superiority of NP-PTX/SIM over both free drugs at 5.25–9.01-fold lower molar doses is uniformly explained by the physicochemical and release properties established in Sections 3.1 and 3.2, notably the 152 ± 5 nm particle size, +31.2 ± 1.5 mV zeta potential, high entrapment efficiency, and sustained anomalous release kinetics, which collectively enable disproportionately high intracellular drug exposure at a sub-11 μg mL^{-1} nominal IC_{50}.[4,5,13,14] The complete pharmacological inertness of blank nanoparticles across all three assays conclusively attributes this multi-mechanistic activity to the co-delivered drug payload.[13,33] These findings were obtained in HCT-116 cells, a well-validated and widely accepted model for colorectal cancer research. While this represents a standard starting point for *in vitro* anticancer evaluation, we acknowledge that testing in additional CRC cell lines with different mutational profiles would further strengthen the generalizability of these mechanistic conclusions. This is identified as a priority objective for future investigation. Collectively, these findings provide rigorous and internally consistent mechanistic validation of the therapeutic strategy, confirming that NP-PTX/SIM operates through genuine apoptotic induction, anti-proliferative suppression, and anti-angiogenic activity, and strongly support its advancement to *in vivo* pharmacodynamic and antitumor efficacy evaluation.

4 Conclusion

This study successfully developed, optimized, and evaluated a novel pH-responsive nanoformulation for the co-delivery of pentoxifylline and simvastatin against colorectal cancer. While the Eudragit S100–chitosan hybrid carrier is an established pH-responsive oral delivery platform, the innovation of this work lies in applying it to this specific repurposed drug combination, supported by systematic QbD optimization and comprehensive *in vitro* and *in silico* validation. The optimized nanoparticles exhibited suitable physicochemical properties and pH-triggered release behavior, demonstrating preferential drug liberation at simulated colonic pH (pH 7.4) *in vitro*, which is consistent with a mechanistic rationale for oral delivery with colonic preference. These *in vitro* findings do not constitute proof of *in vivo* site-specific colon targeting; confirmation of actual colonic drug delivery and therapeutic benefit requires future *in vivo* pharmacokinetic and biodistribution studies. Molecular docking further supported a multi-target mechanism for simvastatin against EGFR, CA9, and GSK3β. The NP-PTX/SIM formulation demonstrated potent cytotoxicity in HCT-116 colorectal cancer cells (IC_{50} = 10.21 μg mL^{-1}), with quantitative Chou–Talalay analysis confirming strong synergism (CI = 0.42), mediated through caspase-3 – dependent apoptosis and suppression of Ki-67 and VEGF biomarkers. As these findings were obtained in a single CRC cell line, the results should be interpreted within this context, and validation in additional models is warranted to confirm broader applicability. Overall, this work bridges pharmaceutical formulation, computational drug discovery, and experimental oncology, supporting the potential of repurposed drug combinations delivered *via* smart polymeric nanocarriers for colorectal cancer therapy.

Future studies will focus on *in vivo* pharmacokinetic, biodistribution, and efficacy evaluation to establish whether the pH-responsive release behavior demonstrated *in vitro* translates to effective preferential colonic drug delivery and therapeutic activity *in vivo*, as well as assessment of synergistic activity in additional CRC cell lines with diverse molecular backgrounds. Beyond PTX/SIM, the Eudragit S100–chitosan ionic gelation system demonstrates inherent versatility due to its physicochemically driven encapsulation mechanism, mild aqueous preparation, scalable processing, and use of GRAS-designated excipients. This platform may therefore be extended to other colorectal cancer chemotherapeutics, including 5-fluorouracil, oxaliplatin, irinotecan, and capecitabine, while the QbD-defined design space established in this study provides a rational framework for rapid optimization of future pH-responsive combination nanoformulations.

Consent for publication

The authors confirm: this work represents original research that has not been previously published in any form; this manuscript has not been submitted for review or publication consideration elsewhere; the publication has received approval from all co-authors.

Author contributions

Samar M. Mahgoub: conceptualization, methodology, investigation, data curation, writing – original draft preparation.

Seham M. Hamed: methodology, supervision, validation, funding. Ahmed A. Allam: formal analysis, data interpretation. Doaa R. I. Abdel-Gawad: methodology, experimental work, validation. Ahmed G. Soliman: software, data analysis. Khaled Metwally: supervision, project administration, writing – review and editing. Rehab Mahmoud: visualization, data interpretation, writing – review and editing.

Conflicts of interest

All authors declare that they have no conflicts of interest to disclose.

Abbreviations

4 PL	Four-parameter logistic
BBD	Box–Behnken experimental design
CQA	Critical quality attribute
CRC	Colorectal cancer
CI	Combination index
DALYs	Disability-adjusted life years
DMSO	Dimethylsulfoxide
DoE	Design of experiments
EE	Encapsulation efficiency
ELISA	Enzyme-linked immunosorbent assay
EPR	Enhanced permeability and retention
FBS	Fetal bovine serum
HCT-116	Human breast adenocarcinoma cells
HPLC	High-performance liquid chromatography
IC_{50}	Half-maximal inhibitory concentration
MTT	3-(4,5-Dimethylthiazol-2-yl)-2,5-diphenyltetrazolium bromide
NF-κB	Nuclear factor kappa-B
PBS	Phosphate-buffered saline
PDI	Polydispersity index
PTX	Pentoxifylline
QbD	Quality by design
SAED	Selected area electron diffraction
SCF	Simulated colonic fluid
SGF	Simulated gastric fluid
SIF	Simulated intestinal fluid
SIM	Simvastatin
TEM	Transmission electron microscopy
TNF-α	Tumor necrosis factor-alpha
TPP	Tripolyphosphate
VEGF	Vascular endothelial growth factor

Data availability

The datasets generated and/or analyzed during this study are available from the corresponding author upon reasonable request.

Supplementary information (SI) is available. See DOI: https://doi.org/10.1039/d6ra02003h.

Acknowledgements

This work was supported and funded by the Deanship of Scientific Research at Imam Mohammad Ibn Saud Islamic University (IMSIU) (grant number IMSIU-DDRSP2601).

References

1 L. Roberts, *Cancer Today: Origins, Prevention, and Treatment*, Institute of Medicine, 1984.
2 M. Arnold, M. S. Sierra, M. Laversanne, I. Soerjomataram, A. Jemal and F. Bray, Global patterns and trends in colorectal cancer incidence and mortality, *Gut*, 2017, **66**, 683–691.
3 M. C. S. Wong, H. Ding, J. Wang, P. S. F. Chan and J. Huang, Prevalence and risk factors of colorectal cancer in Asia, *Intest. Res.*, 2019, **17**, 317–329.
4 P. R. Raikar, P. M. Dandagi and V. M. Kumbar, An innovative synergistic combination using eudragit-coated galactosylated PLGA-pluronic nanoparticles for addressing colorectal cancer, *J. Drug Delivery Sci. Technol.*, 2024, **94**, 105481, DOI: 10.1016/j.jddst.2024.105481.
5 W. Mu, Q. Chu, Y. Liu and N. Zhang, A review on nano-based drug delivery system for cancer chemoimmunotherapy, *Nano-Micro Lett.*, 2020, **12**, 142.
6 O. A. Ala, *Perspective Chapter: Statins Use in Cancer Treatment–Unraveling the Mechanisms and Future Therapeutic*, Frontiers, 2025.
7 M. Dobrzycka, P. Spychalski, A. J. Łachiński, P. Kobiela, P. Jędrusik and J. Kobiela, Statins and colorectal cancer–a systematic review, *Exp. Clin. Endocrinol. Diabetes*, 2020, **128**, 255–262.
8 Y. Dang, Y. Zhang and Z. Wang, The role of statins in the regulation of breast and colorectal cancer and future directions, *Front. Pharmacol*, 2025, **16**, 1578345, DOI: 10.3389/fphar.2025.1578345.
9 Y. Shirakami, T. Kochi, M. Kubota, H. Sakai, T. Ibuka, K. Yoshimi, T. Kuramoto, T. Tanaka, M. Shimizu and M. Seishima, Inhibitory effects of pentoxifylline on inflammation-related tumorigenesis in rat colon, *Oncotarget*, 2018, **9**, 33972.
10 B. A. Al-Husein, N. M. Mhaidat, K. H. Alzoubi, G. M. Alzoubi, M. A. Y. Alqudah, A. M. Albsoul-Younes and S. M. Matalqah, Pentoxifylline induces caspase-dependent apoptosis in colorectal cancer cells, *Inform. Med. Unlocked*, 2022, **31**, 100997.
11 G. Golunski, A. Woziwodzka and J. Piosik, Potential Use of Pentoxifylline in Cancer Therapy, *Curr. Pharm. Biotechnol.*, 2018, **19**, 206–216, DOI: 10.2174/1389201019666180528084641.
12 Y. C. C. E. Za, S. Wu, L. Huang, C. Buquet, R. Shen, B. S. G. Nzalez, E. A. G. Latorre, O. Boyer, R. Varin, L. A. Jiménez-Zamudio, A. Janin, J. P. Vannier, H. Li and H. Lu, Synergistic promoting effects of pentoxifylline and simvastatin on the apoptosis of triple-negative MDA-MB-231 breast cancer cells, *Int. J. Oncol.*, 2018, **52**, 1246–1254, DOI: 10.3892/ijo.2018.4272.

13 W. Gonciarz, E. Balcerczak, M. Brzeziński, A. Jeleń, A. J. Pietrzyk-Brzezińska, V. H. B. Narayanan and M. Chmiela, Chitosan-based formulations for therapeutic applications. A recent overview, *J. Biomed. Sci.*, 2025, **32**, 62.
14 H. Choukaife, S. Seyam, B. Alallam, A. A. Doolaanea and M. Alfatama, Current Advances in Chitosan Nanoparticles Based Oral Drug Delivery for Colorectal Cancer Treatment, *Int. J. Nanomed.*, 2022, **17**, 3933–3966, DOI: 10.2147/IJN.S375229.
15 S. J. Kshirsagar, M. R. Bhalekar and R. R. Umap, In vitro in vivo comparison of two pH sensitive Eudragit polymers for colon specific drug delivery, *J. Pharmaceut. Sci. Res.*, 2009, **1**, 61.
16 G. Wang, Y. Yang, D. Yi, L. Yuan, P.-H. Yin, X. Ke, W. Jun-Jie and M.-F. Tao, Eudragit S100 prepared pH-responsive liposomes-loaded betulinic acid against colorectal cancer in vitro and in vivo, *J. Liposome Res.*, 2022, **32**, 250–264.
17 N. K. Sahu and N. K. Lariya, pH-responsive Eudragit® S-100 coated chitosan nanoparticles for targeted curcumin delivery in ulcerative colitis: formulation and optimization, *Int. J. Appl. Pharm.*, 2025, **17**, 252–259.
18 S. M. Mahgoub, M. A. Alwaili, H. A. Rudayni, M. A. Almalki, A. A. Allam, M. A. Abdel-Reheim, O. A. Mohammed and M. A. Mohamed, Eco-friendly RP-HPLC approach for simultaneously estimating the promising combination of pentoxifylline and simvastatin in therapeutic potential for breast cancer: Appraisal of greenness, whiteness, and Box–Behnken design, *Green Process. Synth.*, 2024, **13**, 20240139.
19 M. Rao, Y. Mandage, K. Thanki and S. Bhise, Dissolution improvement of simvastatin by surface solid dispersion technology, *Dissolution Technol.*, 2010, **17**, 27–34.
20 M. Shah and K. Pathak, Development and statistical optimization of solid lipid nanoparticles of simvastatin by using 23 full-factorial design, *AAPS PharmSciTech*, 2010, **11**, 489–496.
21 M. Verheijen, M. Lienhard, Y. Schrooders, O. Clayton, R. Nudischer, S. Boerno, B. Timmermann, N. Selevsek, R. Schlapbach and H. Gmuender, DMSO induces drastic changes in human cellular processes and epigenetic landscape in vitro, *Sci. Rep.*, 2019, **9**, 4641.
22 K. Summer, J. Browne, M. Hollanders and K. Benkendorff, Out of control: The need for standardised solvent approaches and data reporting in antibiofilm assays incorporating dimethyl-sulfoxide (DMSO), *Biofilm*, 2022, **4**, 100081.
23 A. S. McKim and R. Strub, Dimethyl sulfoxide USP, PhEur in approved pharmaceutical products and medical devices, *Pharmaceut. Technol.*, 2008, **32**, 74.
24 E. Schultze, K. Coradini, P. dos Santos Chaves, L. P. da Silva, J. Buss, S. S. Guterres, T. Collares, R. C. R. Beck, A. R. Pohlmann and F. K. Seixas, Drug-loaded nanoemulsion as positive control is an alternative to DMSO solutions for in vitro evaluation of curcumin delivery to MCF-7 cells, *Pharmacol. Rep.*, 2017, **69**, 1408–1412.
25 M. Sethi, R. Sukumar, S. Karve, M. E. Werner, E. C. Wang, D. T. Moore, S. R. Kowalczyk, L. Zhang and A. Z. Wang, Effect of drug release kinetics on nanoparticle therapeutic efficacy and toxicity, *Nanoscale*, 2014, **6**, 2321–2327.
26 S. D'Souza, A review of in vitro drug release test methods for nano-sized dosage forms, *Adv. Pharmaceut.*, 2014, **2014**, 304757.
27 T. Mosmann, Rapid colorimetric assay for cellular growth and survival: application to proliferation and cytotoxicity assays, *J. Immunol. Methods*, 1983, **65**, 55–63.
28 E. A. Abdelsalam, A. A. Abd El-Hafeez, W. M. Eldehna, M. A. El Hassab, H. M. M. Marzouk, M. M. Elaasser, N. A. Abou Taleb, K. M. Amin, H. A. Abdel-Aziz and P. Ghosh, Discovery of novel thiazolyl-pyrazolines as dual EGFR and VEGFR-2 inhibitors endowed with in vitro antitumor activity towards non-small lung cancer, *J. Enzyme Inhib. Med. Chem.*, 2022, **37**, 2265–2282.
29 M. F. Abo-Ashour, W. M. Eldehna, A. Nocentini, A. Bonardi, S. Bua, H. S. Ibrahim, M. M. Elaasser, V. Kryštof, R. Jorda and P. Gratteri, 3-Hydrazinoisatin-based benzenesulfonamides as novel carbonic anhydrase inhibitors endowed with anticancer activity: Synthesis, in vitro biological evaluation and in silico insights, *Eur. J. Med. Chem.*, 2019, **184**, 111768.
30 T.-C. Chou, Theoretical basis, experimental design, and computerized simulation of synergism and antagonism in drug combination studies, *Pharmacol. Rev.*, 2006, **58**, 621–681, DOI: 10.1124/pr.58.3.10.
31 J. L. do Nascimento, M. C. V. da Costa, L. F. de Macêdo, L. H. C. de Macêdo, R. O. de Moura, T. J. A. de Mélo, W. R. V. da Rocha, A. C. F. de Melo Costa, J. L. Soares-Sobrinho and D. T. C. da Silva, Laponite®-based smart hydrogels for sustained topical delivery of silver sulfadiazine: a strategy for the treatment of contaminated or biofilm-forming wounds, *Pharmaceutics*, 2025, **17**, 1234.
32 F. Ahmadi, Z. Oveisi, S. M. Samani and Z. Amoozgar, Chitosan based hydrogels: characteristics and pharmaceutical applications, *Res. Pharm. Sci.*, 2015, **10**, 1–16.
33 S. Thakral, N. K. Thakral and D. K. Majumdar, Eudragit®: a technology evaluation, *Expert Opin. Drug Deliv.*, 2013, **10**, 131–149.
34 A. Rampino, M. Borgogna, P. Blasi, B. Bellich and A. Cesàro, Chitosan nanoparticles: Preparation, size evolution and stability, *Int. J. Pharm.*, 2013, **455**, 219–228.
35 A. Bernkop-Schnürch and S. Dünnhaupt, Chitosan-based drug delivery systems, *Eur. J. Pharm. Biopharm.*, 2012, **81**, 463–469.
36 A. Akhgari, F. Farahmand, H. A. Garekani, F. Sadeghi and T. F. Vandamme, Permeability and swelling studies on free films containing inulin in combination with different polymethacrylates aimed for colonic drug delivery, *Eur. J. Pharm. Sci.*, 2006, **28**, 307–314.
37 K. G. H. Desai and H. Jin Park, Recent developments in microencapsulation of food ingredients, *Dry. Technol.*, 2005, **23**, 1361–1394.
38 F. Siepmann, J. Siepmann, M. Walther, R. J. MacRae and R. Bodmeier, Polymer blends for controlled release coatings, *J. Controlled Release*, 2008, **125**, 1–15.

39 C. N. Patra, R. Priya, S. Swain, G. K. Jena, K. C. Panigrahi and D. Ghose, Pharmaceutical significance of Eudragit: A review, *Future J. Pharmaceut. Sci.*, 2017, **3**, 33–45.
40 J. J. Wang, Z. W. Zeng, R. Z. Xiao, T. Xie, G. L. Zhou, X. R. Zhan and S. L. Wang, Recent advances of chitosan nanoparticles as drug carriers, *Int. J. Nanomed.*, 2011, 765–774.
41 N. A. Peppas and J. J. Sahlin, A simple equation for the description of solute release. III. Coupling of diffusion and relaxation, *Int. J. Pharm.*, 1989, **57**, 169–172.
42 S. Dash, P. N. Murthy, L. Nath and P. Chowdhury, Kinetic modeling on drug release from controlled drug delivery systems, *Acta Pol. Pharm.*, 2010, **67**, 217–223.
43 P. Costa and J. M. S. Lobo, Modeling and comparison of dissolution profiles, *Eur. J. Pharm. Sci.*, 2001, **13**, 123–133.
44 T. Higuchi, Mechanism of sustained-action medication. Theoretical analysis of rate of release of solid drugs dispersed in solid matrices, *J. Pharm. Sci.*, 1963, **52**, 1145–1149.
45 J. Siepmann and N. A. Peppas, Higuchi equation: Derivation, applications, use and misuse, *Int. J. Pharm.*, 2011, **418**, 6–12.
46 R. W. Korsmeyer, R. Gurny, E. Doelker, P. Buri and N. A. Peppas, Mechanisms of solute release from porous hydrophilic polymers, *Int. J. Pharm.*, 1983, **15**, 25–35.
47 P. L. Ritger and N. A. Peppas, A simple equation for description of solute release II. Fickian and anomalous release from swellable devices, *J. Controlled Release*, 1987, **5**, 37–42.
48 N. A. Peppas, P. Bures, W. S. Leobandung and H. Ichikawa, Hydrogels in pharmaceutical formulations, *Eur. J. Pharm. Biopharm.*, 2000, **50**, 27–46.
49 J. Siepmann and F. Siepmann, Mathematical modeling of drug delivery, *Int. J. Pharm.*, 2008, **364**, 328–343.
50 C.-C. Lin and A. T. Metters, Hydrogels in controlled release formulations: network design and mathematical modeling, *Adv. Drug Delivery Rev.*, 2006, **58**, 1379–1408.
51 P. Colombo, R. Bettini, P. Santi and N. A. Peppas, Swellable matrices for controlled drug delivery: gel-layer behaviour, mechanisms and optimal performance, *Pharmaceut. Sci. Technol. Today*, 2000, **3**, 198–204.
52 X. Huang and C. S. Brazel, On the importance and mechanisms of burst release in matrix-controlled drug delivery systems, *J. Controlled Release*, 2001, **73**, 121–136.
53 Y. Fu and W. J. Kao, Drug release kinetics and transport mechanisms of non-degradable and degradable polymeric delivery systems, *Expert Opin. Drug Deliv.*, 2010, **7**, 429–444.
54 D. R. Paul and S. K. McSpadden, Diffusional release of a solute from a polymer matrix, *J. Membr. Sci.*, 1976, **1**, 33–48.
55 S. N. Rao, M. S. Head, A. Kulkarni and J. M. LaLonde, Validation studies of the site-directed docking program LibDock, *J. Chem. Inf. Model.*, 2007, **47**, 2159–2171.
56 A. E. Cho, V. Guallar, B. J. Berne and R. Friesner, Importance of accurate charges in molecular docking: quantum mechanical/molecular mechanical (QM/MM) approach, *J. Comput. Chem.*, 2005, **26**, 915–931.
57 D. Gheidari, M. Mehrdad and Z. Karimelahi, Virtual screening, ADMET prediction, molecular docking, and dynamic simulation studies of natural products as BACE1 inhibitors for the management of Alzheimer's disease, *Sci. Rep.*, 2024, **14**, 26431.
58 S. B. Nabuurs, M. Wagener and J. De Vlieg, A flexible approach to induced fit docking, *J. Med. Chem.*, 2007, **50**, 6507–6518.
59 W. Xie, M. Peng, Y. Liu, B. Zhang, L. Yi and Y. Long, Simvastatin induces pyroptosis via ROS/caspase-1/GSDMD pathway in colon cancer, *Cell Commun. Signal.*, 2023, **21**, 329.
60 Q. Liu, H. Xia, S. Zhou, Q. Tang, J. Zhou, M. Ren and F. Bi, Simvastatin inhibits the malignant behaviors of gastric cancer cells by simultaneously suppressing YAP and β-catenin signaling, *OncoTargets Ther.*, 2020, 2057–2066.
61 B. J. Bałan, U. Demkow, P. Skopiński, M. Bychawska, E. Skopińska-Różewska, S. Lewicki and R. Zdanowski, The effect of pentoxifylline on L-1 sarcoma tumor growth and angiogenesis in Balb/c mice, *Cent. Eur. J. Immunol.*, 2017, **42**, 131–139.
62 J. M. Lerma-Díaz, G. Hernández-Flores, J. R. Domínguez-Rodríguez, P. C. Ortíz-Lazareno, P. Gómez-Contreras, R. Cervantes-Munguía, D. Scott-Algara, A. Aguilar-Lemarroy, L. F. Jave-Suárez and A. Bravo-Cuellar, In vivo and in vitro sensitization of leukemic cells to adriamycin-induced apoptosis by pentoxifylline: Involvement of caspase cascades and IκBα phosphorylation, *Immunol. Lett.*, 2006, **103**, 149–158.
63 C. C. Cruz-Galvez, P. C. Ortiz-Lazareno, E. J. Pedraza-Brindis, M. M. Villasenor-Garcia, E. Reyes-Uribe, A. Bravo-Hernandez, R. A. Solis-Martinez, M. Cancino-Marentes, C. Rodriguez-Padilla, A. Bravo-Cuellar and G. Hernandez-Flores, Pentoxifylline Enhances the Apoptotic Effect of Carboplatin in Y79 Retinoblastoma Cells, *In Vivo*, 2019, **33**, 401–412, DOI: 10.21873/invivo.11487.
64 A. Bravo-Cuellar, P. C. Ortiz-Lazareno, E. Sierra-Diaz, F. Solorzano-Ibarra, A. S. Méndez-Clemente, A. Aguilar-Lemarroy, L. F. Jave-Suárez, E. Ruiz Velazco-Nino and G. Hernandez-Flores, Pentoxifylline sensitizes cisplatin-resistant human cervical cancer cells to cisplatin treatment: involvement of mitochondrial and NF-kappa B pathways, *Front. Oncol.*, 2020, **10**, 592706.
65 J. Marcinkiewicz, A. Grabowska, R. Lauterbach and M. Bobek, Differential effects of pentoxifylline, a non-specific phosphodiesterase inhibitor, on the production of IL-10, IL-12 p40 and p35 subunits by murine peritoneal macrophages, *Immunopharmacology*, 2000, **49**, 335–343.